Crystal fabric development and slip systems in a quartz mylonite: an approach via transmission electron microscopy and viscoplastic self-consistent modelling

Luiz F.G. Morales, David Mainprice, Geoffrey E Lloyd, Richard Law

▶ To cite this version:

Luiz F.G. Morales, David Mainprice, Geoffrey E Lloyd, Richard Law. Crystal fabric development and slip systems in a quartz mylonite: an approach via transmission electron microscopy and viscoplastic self-consistent modelling. David J. Prior; Ernest H. Rutter; Daniel J. Tatham. Deformation Mechanisms, Rheology and Tectonics: Microstructures, Mechanics and Anisotropy, 360, Geological Society of London, pp.153-173, 2011, Geological Society Special Publications, 10.1144/SP360.9 . hal-00688840

Crystal fabric development and slip systems in a quartz mylonite: an approach via transmission electron microscopy and viscoplastic self-consistent modelling

LUIZ F. G. MORALES[1]*, DAVID MAINPRICE[1], GEOFFREY E. LLOYD[2] &
RICHARD D. LAW[3]

[1]*Géosciences Montpellier UMR CNRS 5243 & Université Montpellier 2,
Place Eugène Bataillon, Batîment 22, 34095, Montpellier cedex 05, France*

[2]*Institute of Geophysics and Tectonics, School of Earth and Environment,
University of Leeds, Leeds LS2 9JT, UK*

[3]*Department of Geosciences, Virginia Tech., Blacksburg, VA, 24061, USA*

**Corresponding author (e-mail: luiz_grafulha@yahoo.com.br)*

Abstract: We have applied transmission electron microscopy (TEM) analyses coupled with viscoplastic self-consistent (VPSC) numerical modelling to identify the active slip systems and to better understand the crystal preferred orientation (CPO) development of the Torridon quartz mylonite (NW Scotland). TEM analyses showed evidence of activation of $1/3\langle a\rangle\{\pi'\}$, $1/3\langle a\rangle\{z\}$ and possible $\langle a\rangle(c)$ slip systems, as well as dislocation climb and dynamic recrystallization. All the CPOs generated by VPSC models share common characteristics with the Torridon quartz mylonite, but only Models 2 and 3 reproduce the $[c]$-axes maxima at low angle ($<20^\circ$) to the foliation pole along the *YZ* plane, as observed in the mylonite. In Model 2, this concentration only occurs at $\gamma \geq 2.6$, whereas in Model 3 this maxima occurs at lower shear strains. The models that start with a previous preferred orientation acquire very strong CPOs after small-imposed strains, followed by the rapid rotation of the fabric in relation to the new imposed finite strain axes. The combined activation of $\langle a\rangle\{\pi'\}$, $\langle a\rangle\{z\}$ and possibly $\langle a\rangle(c)$ slip systems, as demonstrated by TEM analyses, suggests that the VPSC model that best predicts CPO development in the Torridon quartz mylonite is Model 2, where the critical resolved shear stress (CRSS) of $\langle a\rangle\{\pi/\pi'\}$ is assumed to be slightly stronger than $\langle a\rangle(c)$.

Quartz mylonites are typical rocks of high-strain zones and result from localized deformation in quartzites and quartz veins and by the intense deformation of granitoids in the presence of fluids under upper to middle-crustal conditions (e.g. Dixon & Williams 1983; Law *et al.* 1986, 1990; Lloyd *et al.* 1992; Fitz Gerald & Stünitz 1993; Goodwin & Wenk 1995; Hippertt 1998; Wibberley 1999; Lloyd 2004; Jefferies *et al.* 2006; Pennacchioni *et al.* 2010). Less common but no less important is the occurrence of quartz mylonites in the lower crust, suggesting high differential stresses for their generation and implying a contrasting geological behaviour for the lower crust under certain conditions (e.g. Fitz Gerald *et al.* 2006). In all of these cases, quartz mylonites play an important role in controlling lithospheric strength as they may allow deformation localization (e.g. Carter & Tsenn 1987). Independently of the processes in which the quartz mylonites are generated, a common feature observed in these rocks is the development of strong crystal preferred orientation (CPO) of quartz. Quartz CPOs can be used to infer deformation temperatures, magnitude and symmetry of strain and kinematic framework and the mechanisms for deformation (e.g. Schmid & Casey 1986; Law 1990; Stipp *et al.* 2002; Law *et al.* 2004). The development of CPO usually implies the activation of dislocation creep. CPO patterns are usually interpreted in terms of the relative activation of different slip systems, essentially controlled by temperature and variation in the strain and kinematic conditions (e.g. Schmid & Casey 1986; Okudaira *et al.* 1995; Takeshita 1996; Kurz *et al.* 2002; Heilbronner & Tullis 2006). Nevertheless, quartz CPOs depart from these expected patterns in many cases given the deformation conditions of certain rocks, and their interpretation by purely intracrystalline plasticity mechanisms is not straightforward (e.g. Hippertt 1998). Mechanisms such as dynamic recrystallization, dissolution/precipitation, grain-boundary sliding and diffusion creep have also been used to explain the variety of quartz fabrics observed in both nature and experiments (e.g.

Wenk & Christie 1991; Gleason *et al.* 1993; Hippertt & Egydio-Silva 1996; van Daalen *et al.* 1999; Heilbronner & Tullis 2002, 2006; Stipp *et al.* 2002; Halfpenny *et al.* 2006; Vernooij *et al.* 2006). In addition, CPO patterns are typically a 'post-mortem' feature for which we usually do not know the deformation path that produced the preferred orientation.

In general, CPO patterns are interpreted assuming initially randomly distributed crystal orientations in a volume of rock prior to deformation. This deformation, and the mechanisms responsible for its accommodation, is responsible for the development of a given CPO. Indeed, in many cases this is what happens (e.g. Pennacchioni *et al.* 2010). In other cases, for example, the assumption has to be made simply because of the lack of exposure from low- to high-strain conditions along a shear zone. The role of pre-existing CPO on fabric development in high-strain zones is only rarely considered (e.g. Lister & Williams 1979; Ralser *et al.* 1991; Lloyd *et al.* 1992; Toy *et al.* 2008; Pennacchioni *et al.* 2010). Such 'initial' CPOs may have a strong influence on the 'final' CPO patterns observed in shear-zone mylonites.

The quartz mylonite studied here originated from intense simple-shear deformation of a quartz-feldspar vein infilling a joint in Lewisian gneiss of the Upper Loch Torridon area (NW Scotland). This vein is perhaps one of the most-studied quartz-bearing mylonites in terms of microstructures and preferred orientations (Law *et al.* 1990; Lloyd *et al.* 1992; Trimby *et al.* 1998; Lloyd 2004; Lloyd & Kendall 2005). Nevertheless, specific points regarding the nature and evolution of the CPO of the mature mylonite (centre of the vein/shear zone) and its relation to the CPO of the original quartz vein (now only preserved at the margins of the quartz vein/shear-zone walls) remain poorly constrained. Specifically, it is not well understood whether the crystallographic orientation observed in the mature mylonite is the result of a single episode of deformation dominated by single or multiple slip systems (Law *et al.* 1990) or if the observed preferred orientation reflects an inherited initial fabric from the margin of the sheared quartz vein (Lloyd *et al.* 1992). The preferred orientation observed in the quartz mylonite from Torridon cannot be solely explained by intra-crystalline plasticity via mutual activation of basal, rhomb and prismatic slip in the $\langle a \rangle$ direction, as commonly observed in quartz-rich tectonites deformed at relatively low temperatures (e.g. samples R-405, P-248 and C-156 of Schmid & Casey 1986); other mechanisms have to be active, such as Dauphiné twinning and dynamic recrystallization (Law *et al.* 1990; Lloyd *et al.* 1992; Trimby *et al.* 1998; Lloyd 2004). The Torridon quartz mylonite is therefore a good case study for testing, through systematic modelling of crystallographic fabric development via the viscoplastic self-consistent (VPSC) approach (Lebensohn & Tomé 1993; Tomé & Lebensohn 2004), whether CPO results from a single deformation episode (starting from a random orientation) or if the observed CPO is inherited from the margin of the sheared vein. To better constrain the CPO predictions by numerical modelling, transmission electron microscopy (TEM) images from the mature mylonite are also presented, providing new information regarding the microstructural evolution of this shear zone and complementing previous work carried out by Law *et al.* (1990), Lloyd *et al.* (1992), Trimby *et al.* (1998), Lloyd (2004) and Lloyd & Kendall (2005).

Sample description and quartz CPO

The quartz feldspar vein from the head of Upper Loch Torridon (Fig. 1a, b) was sheared during relative motion of joint blocks of Lewisian gneiss on either side of the vein. Foliation (XY) associated with shearing increases in intensity traced in to the centre of the vein and simultaneously curves towards parallelism with the vein/shear-zone margins (*sensu* Ramsay & Graham 1970) but is still inclined at 9° to the shear-zone margins in the 'mature' high-strain centre of the vein (Law *et al.* 1990). Original vein textures are only locally preserved at the low-strain margins of the vein. The high-strain centre of the vein is characterized by a typical Type-2 S–C′ microstructure (Law *et al.* 1990).

The vein microstructure is arranged in two planar domains aligned parallel to the macroscopic foliation. One domain consists of elongate dynamically recrystallized quartz grains (<100 μm) whose long axes are oblique to the main foliation, while the second domain is characterized by an equigranular texture of quartz and feldspar with grain size of less than 5 μm. The microstructure suggests that deformation occurred under constant-volume plane strain flow conditions very close to strict simple shear (Law *et al.* 1990; Wallis 1995, p. 1082). A band-contrast electron backscatter diffraction (EBSD) map (Fig. 1a) and cathodoluminescence (CL) image (Fig. 1b) illustrate development of the shear zone with a spatially rapid development of foliation, grain-size reduction and fracturing of feldspar crystals within the quartz matrix. The mature mylonite (MM) in the centre of the vein consists of dynamically recrystallized grains originating from a few larger grains preserved at the vein margins (Lloyd *et al.* 1992; Trimby *et al.* 1998). Close inspection of the boundary of the quartz vein material at the margins of the vein (starting

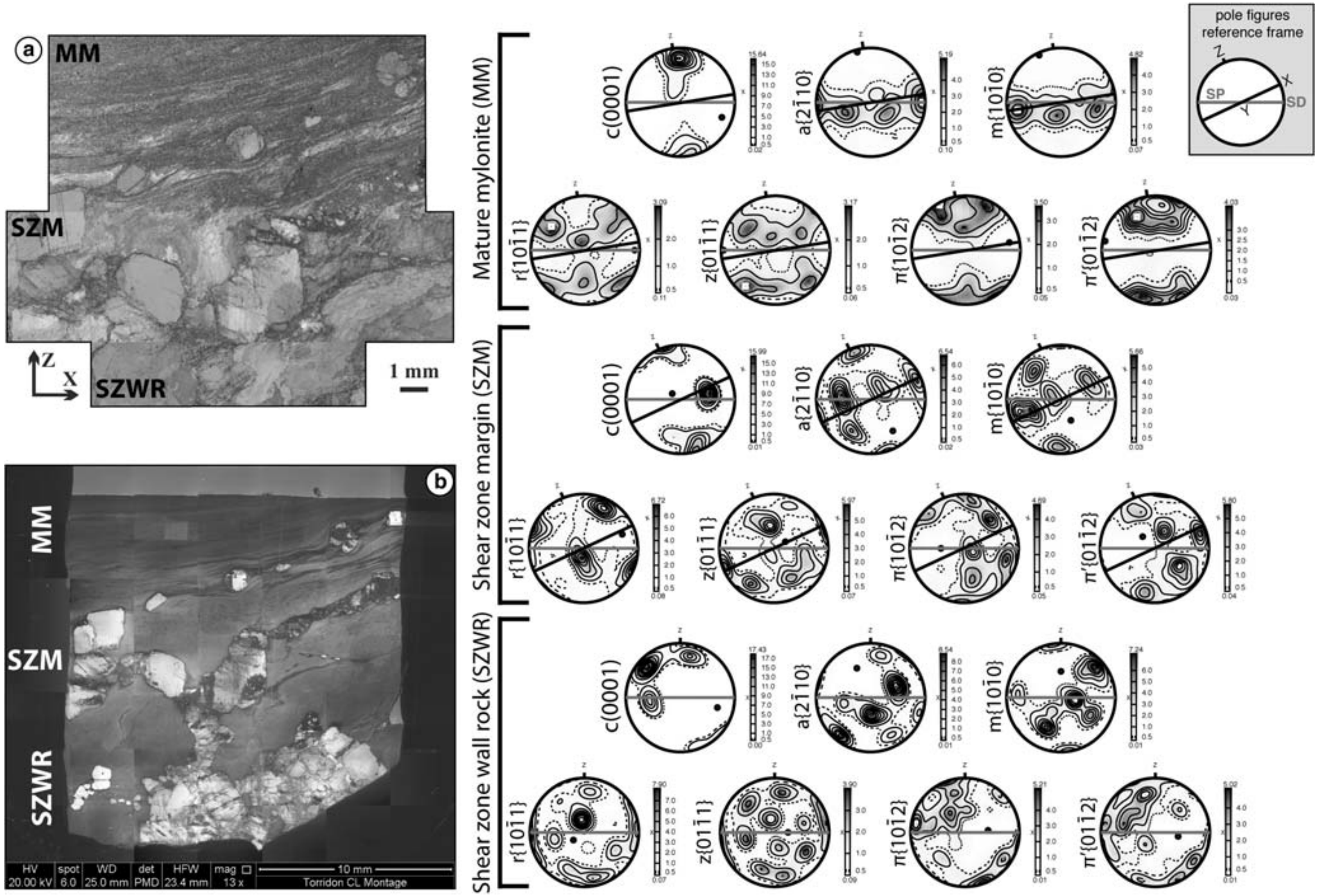

Fig. 1. SEM/EBSD images of the Torridon Shear Zone (*XZ* plane) include (**a**) a digital band contrast map in which the greyscale reflects the quality of the electron back-scattered patterns (bright: good EBSPs; dark: weak EBSPs) and (**b**) a cathodoluminescence (CL) image (montage of multiple scans) of the whole sample. Both images reveal detailed features of the microstructures, including: grain-size reduction over a short distance; mylonitic foliation development; and foliation deflection and brittle behaviour of feldspars. (**c**) Pole figures from EBSD maps for the shear-zone wall rock (SZWR), shear-zone margin (SZM) and mature mylonite (MM). Pole figures are plotted in shear-zone margin reference frame, represented here by the horizontal east–west plane (horizontal line). Note in the microstructural images that the foliation is inclined *c*. 9° anticlockwise in relation to the reference east–west plane, as marked by the black line in the pole figures (see reference frame in inset). Lower hemisphere, equal-area projections, multiples of uniform distribution, MAD = 1.3°. Figure (a) modified from Lloyd (2004).

material) and mature mylonite in the centre of the vein/shear zone revealed the presence of abundant Dauphine twinning in narrow intra-granular 'bands' (Lloyd 2004).

A comparison between the pole figures of different parts of the shear zone suggest a rapid spatial transition of the quartz CPO between the original vein material at the margin of the vein/shear zone and the mature mylonite in the centre of the shear zone, in agreement with the observed microstructures. Note that all the pole figures in Figure 1 were plotted with the shear-zone margin as the reference plane, where the foliation of the mature mylonite is inclined *c*. 9° anticlockwise in relation to this reference plane (inset diagram in Fig. 1). In the shear-zone wall rock, the quartz *c* (0001)-axes are distributed in one dominant and two secondary single maxima (Fig. 1) at angles between 30 and 60° to each other; the dominant maxima lies at an angle of *c*. 45° from the pole to the shear plane. The poles for the first *m* $\{10\bar{1}0\}$ and second *a* $\{2\bar{1}10\}$ order prisms are distributed in three dominant point maxima forming a great circle girdle whose pole is the strongest concentration of [*c*]-axes. The poles to positive rhombs *r* $\{10\bar{1}1\}$ are strongly concentrated near the centre of the stereonet (sample *Y* direction), while the poles to negative rhomb *z* $\{01\bar{1}1\}$ are distributed in ten distinct maxima distributed over the equal-area net. The poles to acute rhombs π $\{10\bar{1}2\}$ and π' $\{01\bar{1}2\}$ are distributed along small circle (conical) girdles around the [*c*]-axes maxima.

The [*c*]-axes in the shear-zone margin occur in two maxima where the dominant maximum lies between *X* and *Y* and the secondary maximum lies on the primitive circle of the net, making an angle of *c*. 20° with the pole of the shear-zone margin. The poles to $\{m\}$ and $\{a\}$ prisms are distributed in five maxima, and the dominant maximum lies in the shear plane or at a low angle to it in the opposite direction to the [*c*]-maxima. The poles to $\{r\}$, $\{z\}$, $\{\pi\}$ and $\{\pi'\}$ are roughly distributed as three maxima, where the rhombs $\{r\}$ and acute rhomb $\{\pi'\}$ define the 'single-crystal' like character of the CPO in the shear-zone margin.

In the mature mylonite (Fig. 1) the [*c*]-axes are distributed along a discontinuous symmetric single girdle, normal to the shear-zone margin (shear plane) pole and oblique to the mylonitic foliation, with a maximum concentration lying *c*. 18° from the shear plane pole towards the centre of the stereonet. The poles to prisms $\{m\}$ and $\{a\}$ are distributed along single girdles parallel to the shear plane, both with three distinct maxima reflecting the three symmetric $\langle a\rangle$ and $\langle m\rangle$-directions dictated by crystallography where the $\langle a\rangle$-directions were equally efficient as the dominant slip direction. The poles of acute rhomb ($\{\pi\}$, $\{\pi'\}$) and rhomb ($\{r\}$, $\{z\}$) are distributed conically around the maxima of [*c*]-axes with opening angles of 28° for the former and between 52 and 57° for the latter.

Transmission electron microscopy

For TEM-based microstructural analyses of the mature mylonite, selected areas of a thin section similar to the sample T1 of Law *et al.* (1990), Lloyd *et al.* (1992) and Lloyd (2004) were thinned by standard argon ion bombardment procedure with an accelerating voltage of 5 kV. These areas were then examined on a JEOL 120 kV transmission electron microscope using conventional bright-field imaging techniques. Dislocation orientations in relation to the crystallographic directions of quartz were characterized by the trace analysis method, in which the orientation of linear and planar features is recorded for a number of goniometer tilt angles, allowing the determination of their directions. The orientation of the Burgers vector (**b**) was determined via the 'invisibility criteria' (e.g. McLaren 1991), in which pure edge and screw dislocation are invisible or in very weak contrast for diffraction vectors (**g**) normal to the Burgers vector ($\mathbf{g} \cdot \mathbf{b} = \mathbf{0}$ **and** $\mathbf{g} \cdot \mathbf{b} \times \mathbf{u} = \mathbf{0}$, where **u** is the line direction of the dislocation). Depending on the angles between the diffraction vectors, the Burgers vector and dislocation line, the contrast in images can vary from moderate to strong as the contrast is proportional to $\mathbf{g} \cdot \mathbf{b} \times \mathbf{u} \neq \mathbf{0}$ even when $\mathbf{g} \cdot \mathbf{b} = \mathbf{0}$ for mixed dislocations. In practice, $\mathbf{g} \cdot \mathbf{b} = \mathbf{0}$ images are very weak when the deviation from the exact Bragg condition ($\mathbf{s} = 0$) is large ($\mathbf{s} > 0$), even when $\mathbf{g} \cdot \mathbf{b} \times \mathbf{u} \neq \mathbf{0}$. Thus, $\mathbf{s} > 0$ was used to characterize the Burgers vectors. Using computer-simulated images of quartz, the symmetry of dislocation images about the dislocation line has been shown to be a useful indicator of the $\mathbf{g} \cdot \mathbf{b} = \mathbf{0}$ condition (Mainprice 1981). When $\mathbf{g} \cdot \mathbf{b} = \mathbf{0}$, the images are symmetric about the dislocation line when $\mathbf{s} = 0$ and very weak when $\mathbf{s} > 0$.

Dislocation analysis in Figure 2 demonstrates that the dislocations are out of contrast for a diffraction vector $\mathbf{g2} = (\bar{1}101)$ ($\mathbf{g2} \cdot \mathbf{b} = 0$), which means that $\mathbf{g2} \perp \mathbf{b}$ (Fig. 2b); however, with $\mathbf{g1}|\mathbf{g3} = (0\bar{1}11)$ they show strong contrast ($\mathbf{g1} \cdot \mathbf{b} = \mathbf{g3} \cdot \mathbf{b} > 0$) (Fig. 2a, c). In the strong-contrast images, the dislocations are asymmetrical about the dislocation line (Fig. 2a, c) whereas they appear symmetrical in the weak-contrast image (Fig. 2b). The variation in dislocation image contrast in Figure 2b is due to crystal bending changing the Bragg conditions from **s** *c*. 0 in the top left to $\mathbf{s} > 0$ in the bottom right, consistent with $\mathbf{g} \cdot \mathbf{b} = 0$. The dislocation lines are essentially parallel to each other and suggest that the structure of quartz controls

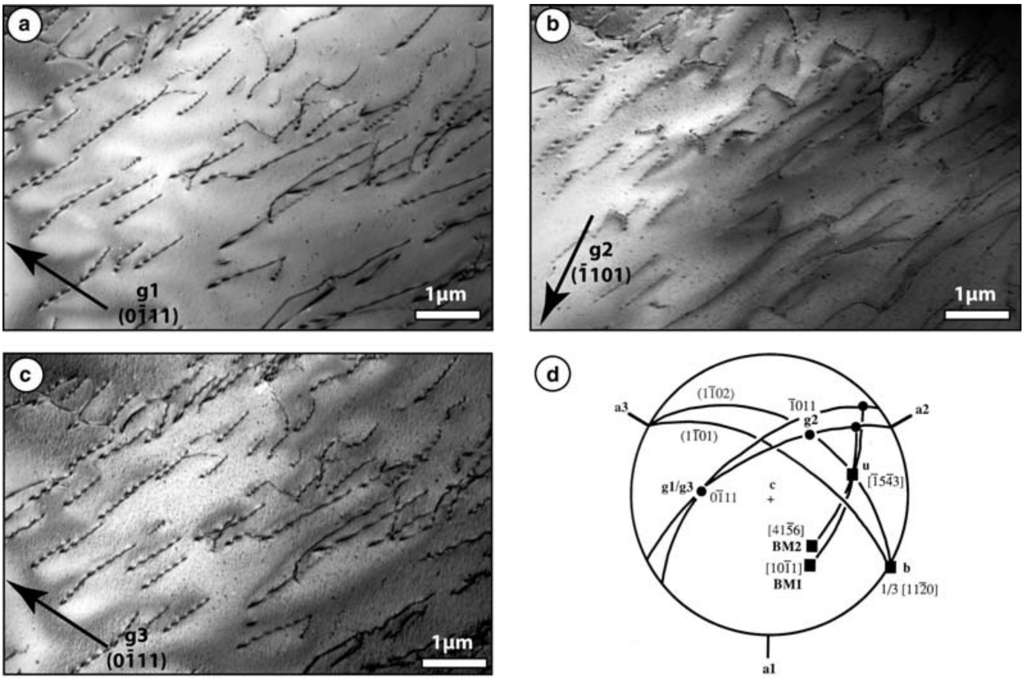

Fig. 2. (**a–c**) Bright-field TEM images of quartz grains at 120 kV in the mature mylonite and (**d**) stereoplot containing the geometrical analysis of dislocations, taking into account two-beam orientation (**BM**), three diffraction vectors (**g1**, **g2**, **g3** – **g1**//**g3**) and the dislocation line direction (**u**). The resultant slip planes and Burgers vector is marked with (b). Dislocations in these pictures are predominantly of mixed-type gliding on π' $(1\bar{1}02)$ plane in ⟨a⟩ $1/3[11\bar{2}0]$ direction.

their orientation. Given the diffraction vectors, the beam orientations ($\mathbf{BM_1} = [10\bar{1}1]$, $\mathbf{BM_2} = [41\bar{5}6]$) and dislocation line direction of $\mathbf{u} = [\bar{1}5\bar{4}3]$ indicated by the tilting procedure, the dislocations of Figure 2 can be described as mixed dislocations with $\mathbf{b} = 1/3[11\bar{2}0]$ (angle between **b** and $\mathbf{u} = 45.73°$) gliding on the $(1\bar{1}02)$ plane (Fig. 2d). Further dislocation analysis presented in Figure 3 using three different diffraction vectors ($\mathbf{g1} = (\bar{1}100)$, $\mathbf{g2} = (01\bar{1}1)$ and $\mathbf{g3} = (10\bar{1}1)$) was impaired by progressive radiation damage in the image and by the extreme variation in contrast of the bright-field images caused by crystal bending. Radiation damage (already visible in Fig. 3c) limited observation time to one zone axis with one beam direction, which does not allow the correct determination of the dislocation line direction **u**. However, most of the long dislocations nearly parallel to the specimen surface are out of contrast for the diffraction vector **g1** ($\mathbf{g1} \cdot \mathbf{b} = 0$), while the contrast is moderate for **g2** ($\mathbf{g2} \cdot \mathbf{b} \neq 0$) and moderate to strong for **g3** ($\mathbf{g3} \cdot \mathbf{b} \neq 0$). The symmetry of the dislocation in the images is not very clear due to crystal bending, but most of them seem to be asymmetric about the dislocation line (as observed in Fig. 3b, c) whereas they are weak and symmetric in Figure 3a, further supporting that $\mathbf{g1} \cdot \mathbf{b} = 0$. When the angles between the trace of the dislocation lines and the diffracting vectors (**g1**, **g2** and **g3**) are taken into account and the Burgers vector $\mathbf{b} = 1/3\ [11\bar{2}0]$ is compatible with the $\mathbf{g} \cdot \mathbf{b}$ values, the two possible line directions are $[\bar{5}4\bar{1}9]$ in the $(1\bar{1}01)$ plane and $[\bar{2}4\bar{2}3]$ in $(1\bar{1}02)$ plane (Fig. 3d). The geometry of dislocations gliding in $(1\bar{1}01)$ with line direction $\mathbf{u} = [\bar{5}4\bar{1}9]$ indicates almost pure edge dislocations (angle **b** to $\mathbf{u} = 87.73°$). Alternatively, the dislocations gliding in $(1\bar{1}02)$ with line direction $\mathbf{u} = [\bar{5}4\bar{1}9]$ may be mixed dislocations (angle **b** to $\mathbf{u} = 64.02°$), similar to the dislocations observed in Figure 2.

The microstructures observed with TEM include subgrain walls (Fig. 4a) and tilt walls, characterized by the regular alignment of parallel straight-edge dislocations. Subgrains are usually slightly elongated (2:1) and have low internal dislocation densities (Fig. 4b). The new grains are also elongate, often with straight boundaries and high densities of dislocations associated with crystal lattice bending (Fig. 4c, d). Dislocation lines in these crystals are either straight or curved, which suggests the lack of structural control on the orientation of

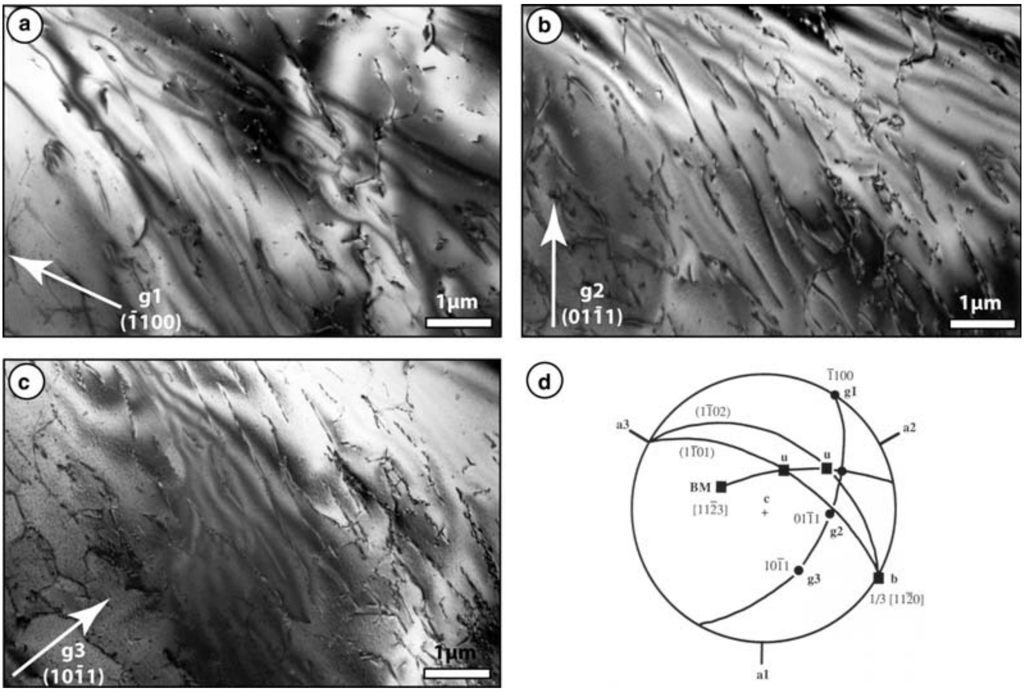

Fig. 3. (**a–c**) Bright-field TEM images of quartz grains at 120 kV in the mature mylonite (**d**) and stereoplot containing the geometrical analysis of dislocations, taking into account one-beam orientation (**BM**), three diffraction vectors (**g1**, **g2**, **g3**) and the dislocation line direction (**u**). The resultant slip planes and Burgers vector is marked with (b). Dislocations in these pictures are predominantly of edge-type gliding on z$(1\bar{1}01)$ plane or mixed type in gliding in π' $(1\bar{1}02)$ $\langle a\rangle$ $1/3[11\bar{2}0]$ direction. Note the beam damage in (c).

dislocation lines at this scale. In some places, dislocations are piled up along crystal boundaries (Fig. 4c), suggesting their inability to propagate through grain boundaries or their absorption along these structures. In addition to the development of subgrain walls, bulging features are observed in some places (Fig. 4d). Hexagonal networks of dislocations resembling honeycombs may also be observed in some grains (Fig. 4e, f). Some of these dislocations are out of contrast when $\mathbf{g} = (0\bar{1}10)$, suggesting that these dislocations are of $\langle a\rangle$ or $[c]$-type (Fig. 4e). However, when the diffraction vector is $(2\bar{1}\bar{1}0)$ with the beam direction parallel to the $[c]$-axis of this particular crystal, all the dislocations become visible and indicate that the networks are formed by $\langle a\rangle$ type dislocations in the basal plane of these crystals (Fig. 4f). The presence of such structures implies that, after a certain amount of propagation in the basal plane, the dislocations in the three symmetrical $\langle a\rangle$ directions ($[a_1]$, $[a_2]$ and $[a_3]$) form nodes or triple junctions at 120° to each other and are sessile, and hence can only contribute to deformation by climb (e.g. Trépied *et al.* 1980).

Modelling CPO development in aggregates

In the last 30 years, different numerical approaches have been used to simulate the evolution of CPO in minerals (Etchecopar 1977; Lister *et al.* 1978; Lister & Paterson 1979; Lister & Hobbs 1980; Takeshita & Wenk 1988; Wenk *et al.* 1989; Canova *et al.* 1992; Casey & McGrew 1999; Takeshita *et al.* 1999). For the present paper we have made extensive use of the viscoplastic self-consistent approach (Lebensohn & Tomé 1993; Tomé & Lebensohn 2004) because of its strong physical basis. Although this approach only allows the simulation of CPO development via intra-crystalline slip, a careful comparison between the CPOs measured in natural rocks and those predicted via VPSC modelling can at least verify the likely contribution of dislocation glide.

Different approaches that impose homogeneous stress (Sachs 1928) or strain (Taylor 1938) within the aggregate are often referred to as lower- and upper-bound constraints. In the VPSC approach, both the local stress and strain can be different from the macroscopic quantities. Compatibility in strain and stress equilibrium is only guaranteed at

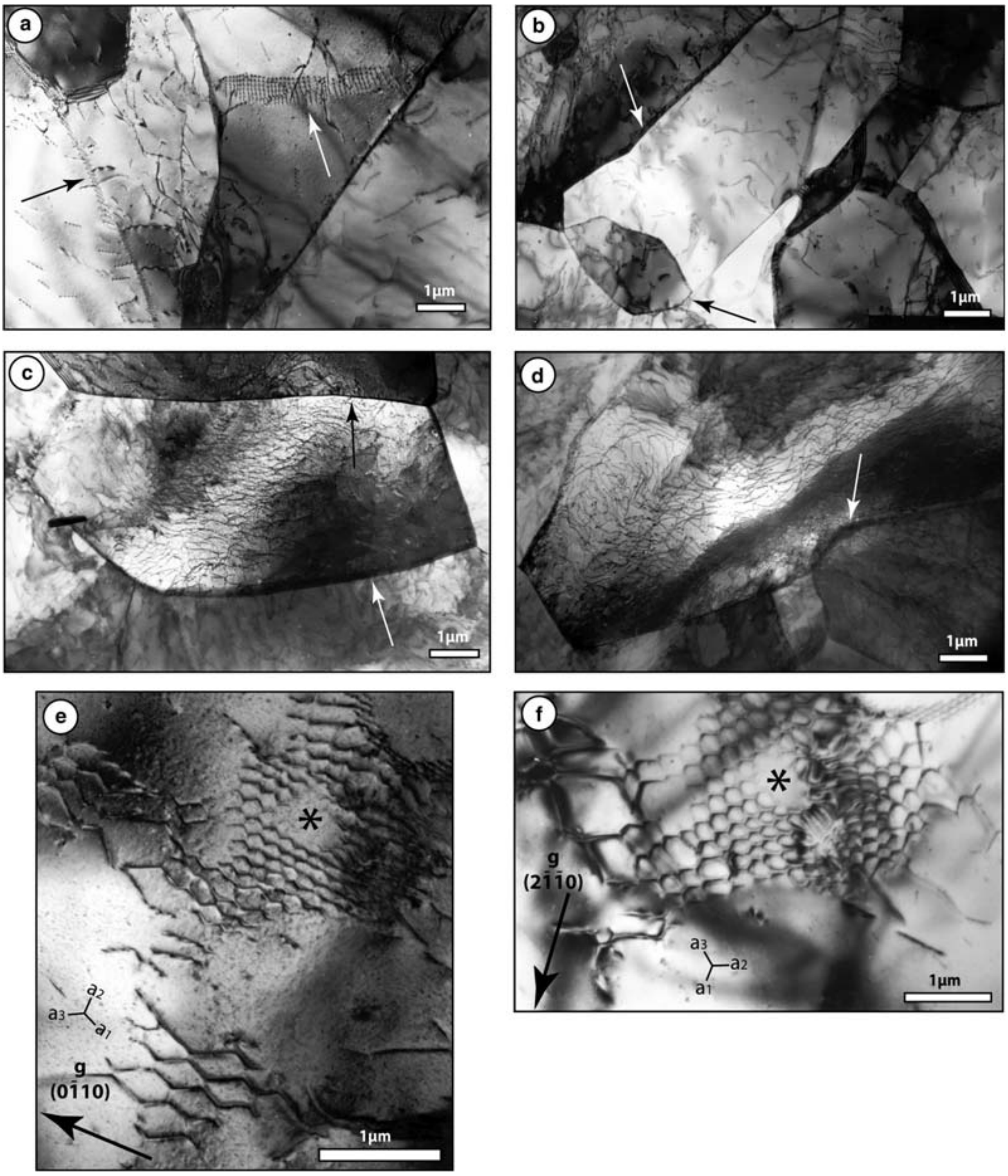

Fig. 4. (**a–c**) Bright-field TEM images of the microstructures of the mature Torridon mylonite include large grains with well-developed subgrains and small grains with high dislocation density. (**a**) Dislocation tilt walls are composed of one family of straight dislocations (marked by the arrows); (**b**) subgrains are either slightly elongated (white arrow) with average aspect ratios of 2:1 or more equant (black arrow); (**c, d**) note the low dislocation density within the subgrains and new elongate grains with high homogeneous dislocation density and variable image contrast due to crystal bending varying the diffraction conditions. Note the straight grain boundaries (black arrow) and the dislocations piled-up along certain boundaries (white arrow) on (c) and bulging feature highlighted by the white arrow on (d). (**e, f**) Hexagonal networks of screw ⟨*a*⟩ dislocations in the basal plane. The triple junctions (nodes) of dislocations are sessile and can only contribute to the deformation by climb. The asterisks are used to locate a common point between the two pictures.

the aggregate scale. Deformation is homogeneous at the grain scale and it is only accommodated by dislocation glide. In addition, the viscoplastic approach used here is spatially disordered, and does not take into account the topology of the aggregate. The shear rate induced in a slip system s by a given local deviatoric stress is described by a viscoplastic law:

$$\dot{\gamma}^s = \dot{\gamma}_0\left(\frac{\tau_r^s}{\tau_0^s}\right) = \dot{\gamma}_0\left(\frac{r_{ij}^s s_{ij}}{\tau_0^s}\right)^{n^s}. \qquad (1)$$

In this equation, $\dot{\gamma}_0$ is the reference strain rate, n^s is the stress exponent (material constant $n = 1$ for Newtonian behaviour such as diffusion creep, $n = 3$ to 5 for dislocation creep), τ_r^s is the critical resolved shear stress (CRSS) and τ_0^s is the stress necessary to activate a given slip system s, whose orientation relative to the stress axes is expressed by its Schmid tensor r^s. The sum of the shear rates over all slip systems gives the grain microscopic strain rate $\dot{\varepsilon}$. To determine the microscopic state for each grain ($\underline{\underline{s}}$, $\dot{\underline{\underline{\varepsilon}}}$) and the volume average that determines the response of the aggregate ($\underline{\underline{\Sigma}}$, $\dot{\underline{\underline{E}}}$; equation (2)), the 'one-site' simplification (Molinari *et al.* 1987; Lebensohn & Tomé 1993) is used in the VPSC formulation:

$$\langle \underline{\underline{s}} \rangle = \underline{\underline{\Sigma}} \quad \langle \dot{\underline{\underline{\varepsilon}}} \rangle = \dot{\underline{\underline{E}}} \qquad (2)$$

Through this method, the interaction between individual grains is not directly taken into account. The interaction between each grain and the surrounding crystals is progressively substituted by the interaction between an inclusion with a crystallographic orientation and an infinite equivalent homogeneous medium (HEM), whose behaviour is the weighted average of the behaviour of the aggregate. The interaction problem can be solved using an equation of Eshelby (1957), which assumes ellipsoidal grain shape and tangential behaviour of HEM:

$$\dot{\varepsilon} - \dot{E}_{ij} = -\alpha\tilde{M}_{ijkl}(s_{kl} - \Sigma_{kl}) \qquad (3)$$

In this equation, $\tilde{M}$ is the interaction tensor that depends on the rheological properties of the aggregate and on the shapes of grains. The quantity α is a constant used to parameterize the interaction between the homogeneous medium and the grains and essentially imposes more or less kinematically rigid conditions on the aggregate. A zero value for α corresponds to the Taylor–Bishop–Hill approach (Taylor 1938; Lister *et al.* 1978). It assumes homogeneous strain within the aggregate and requires the activation of at least five independent slip systems in each crystal to maintain homogeneity in deformation (Lister *et al.* 1978; Lister & Paterson 1979; Lister & Hobbs 1980). The crystals deform at the same rate and have the same shape at each imposed strain step, leading to stress incompatibilities at the grain boundaries which are assumed to be corrected by elastic strains (Wenk *et al.* 1989). On the other hand an α of infinity assumes that all crystals experience the same state of stress (Sachs 1928), which leads to microstructural incompatibility at the grain scale, and strain compatibility is only obtained at the averaged aggregate scale. The classical self-consistent tangent model is given by $\alpha = 1$.

In VPSC models, the evolution of CPO, the activity of slip systems and the aggregate yield strength for a given macroscopic strain history can be calculated from a set of active slip systems, an initial set of orientations and the macroscopic rheological parameters τ_0^s and n^s. For the present paper, the aggregates are composed of 1000 individual orientations. We have modelled crystallographic fabric development starting from random orientations, but also consider a pre-existing preferred orientation as observed at the margins of the Torridon quartz vein. To create a pre-existing crystallographic orientation, we firstly carried out a simple-shear simulation using an initial random orientation dataset, assuming a very low CRSS for the $\langle a\rangle\{\pi'\}$ slip system with the other potential slip systems being virtually inactive, to a shear strain of $\gamma = 1.73$. We then rotated the resultant CPO by an angle of 45° anticlockwise around the centre of the net (finite strain Y-axis), to bring the maximum concentration of $[c]$-axes to the orientation observed in the margin of the sheared quartz vein. A simple-shear deformation was superimposed on this initial CPO up to a shear strain of $\gamma = 1.73$, resulting in a total equivalent strain of 2 ($\gamma = 3.5$). We emphasize that Lloyd *et al.* (1992) mentioned the possibility that the CPO of the mature mylonite could be developed from the intense deformation of a few large grains with an initial orientation. This is not exactly what we modelled here, but at least gives us an idea of how an initial CPO evolves during superimposed deformation.

The deformation history of the aggregate is given by an imposed macroscopic velocity gradient tensor **L**. As the deformation responsible for the CPO development in the mature mylonite in the centre of the sheared quartz vein is thought to be simple shear (Law *et al.* 1990; Wallis 1995), the velocity gradient (L_{ss}) is given by equation (4):

$$L_{\mathrm{ss}} = \begin{bmatrix} 0 & 1 & 0 \\ 0 & 0 & 0 \\ 0 & 0 & 0 \end{bmatrix} \qquad (4)$$

The parameters that can be modified during VPSC modelling are the active slip systems, their critical resolved shear stresses, the stress exponents, the interaction between grains, the HEM (defined by α) and the shapes of grains. The stress exponent for quartz aggregates reported in the literature varies between 1.4 and 5.7 with a mean value of 2.75 (see Mainprice & Jaoul 2009, table 2). In all the VPSC models presented here we used $\alpha = 1$ (tangent model) and a stress exponent of $n^{s} = 3$. The VPSC model is not very sensitive to values of n^{s} between 3 and 5, and almost all minerals except calcite have stress exponents in this range. Increasing the stress exponent results in the strength of CPO becoming more intense for a given finite strain. In our models, the equivalent strain is defined by

$$\varepsilon_{\mathrm{eq}} = \int D_{\mathrm{eq}}(t)\,\mathrm{d}t \qquad (5)$$

where the Von Mises equivalent strain rate is

$$D_{\mathrm{eq}} = \sqrt{\frac{2}{3} D_{ij} D_{ij}}. \qquad (6)$$

Active slip systems in quartz single-crystal and polycrystalline aggregates are constrained by experiments and TEM analyses carried out by a number of authors (e.g. Griggs & Blacic 1965; Baëta & Ashbee 1969; Kronenberg & Tullis 1984; Linker *et al.* 1984; Mainprice & Paterson 1984, 2005; Rutter & Brodie 2004; Mainprice & Jaoul 2009). In our modelling, we have used the slip systems: $a{<}2\bar{1}\bar{1}0{>}c(0001)$; $a{<}2\bar{1}\bar{1}0{>}r\{0\bar{1}11\}$; $a{<}2\bar{1}\bar{1}0{>}z\{01\bar{1}1\}$; $a{<}2\bar{1}\bar{1}0{>}\pi\{0\bar{1}12\}$; $a{<}2\bar{1}\bar{1}0{>}\pi'\{01\bar{1}2\}$; $a{<}2\bar{1}\bar{1}0{>}m\{0\bar{1}10\}$; $c[0001]m\{10\bar{1}0\}$ and $c[0001]a\{2\bar{1}\bar{1}0\}$.

Hard slip systems such as dipyramids with slip directions oblique to both $[c]$ and $\langle a\rangle$ (e.g. $<\bar{2}113>\{10\bar{1}1\}$) are not considered in this paper because VPSC modelling does not require five independent slip systems, unlike the Taylor–Bishop–Hill model. In addition, we do not consider the effect of Dauphiné twinning in our models, but we discuss its possible effects due to the widespread presence of these microstructures in the mature Torridon mylonite (Lloyd 2004).

Evolution of quartz CPO

VPSC simulations from random orientations

For comparison with VPSC models, we have run a lower-bound simulation (e.g. Chastel *et al.* 1993; Tommasi *et al.* 2000) in which simple-shear deformation was accommodated entirely by activation of the $\langle a\rangle\{\pi'\}$ slip system (Fig. 5). For this specific case of single slip, the lower-bound modelling is preferred due to the assumption of homogeneous stress in the aggregate with variable individual crystal strains and represents an ideal end-member case. In these models, the shear plane is vertical (horizontal line) in the pole figures (Figs 5–10) and the shear direction (SD) is horizontal; both are oriented east–west. Foliation is marked by the tilted black line on these pole figures (Figs 5–10). Model 1 (Fig. 6) shows the predicted simple-shear quartz CPO for a postulated set of CRSS values for different slip systems for a deformation occurring under upper greenschist/lower amphibolite facies conditions. In this model, the predominant slip system is $\langle a\rangle(c)$ with activities varying between 40 and 50% as function of strain followed by relatively high activities of rhomb slip $\{r/z\}$ in the $\langle a\rangle$ direction. We emphasize that, in natural or experimental deformation, additional mechanisms such as grain-boundary sliding and grain-boundary migration contribute to achieving strain compatibility. For this reason, the CPO calculated by VPSC modelling is generally stronger for a given strain than that obtained during natural or experimental deformation, because only dislocation glide is considered.

Considering an aggregate of randomly oriented spherical grains of quartz, two possibilities were found for generating high concentrations of quartz *c*-axes in a similar position as the mature Torridon mylonite and the (π') poles near the foliation normal (Z). The first assumes a similar critical resolved shear stress value for $\langle a\rangle(c)$ and $\langle a\rangle\{\pi'\}$ and $\langle a\rangle\{\pi\}$ (Model 2; Fig. 7). The second possibility arises when we assume a much lower CRSS for $\langle a\rangle\{\pi'\}$ and $\langle a\rangle\{\pi\}$ than for $\langle a\rangle(c)$ slip (Model 3; Fig. 8). Dauphiné twinning in trigonal quartz results in the reversal of positive and negative crystallographic forms due a rotation of 60° around the quartz *c*-axis (Frondel 1962). In this situation, the positive and negative rhombs ($\{r/z\}$) and acute rhombs ($\{\pi/\pi'\}$ are in an equal position in relation to the applied stress and, for this reason, all models have the same critical resolved shear stresses for both rhombs and acute rhombs. The models shown in Figures 6–8 have a similar CPO evolution; with increasing strain, the quartz $[c]$-axes are distributed along a symmetric single girdle crossing the reference foliation at Y (but asymmetric in relation to the shear plane). Although the maximum concentration of $[c]$-axes is located near the foliation normal (Z) in Models 2 and 3 (Figs 7 & 8), it is exactly parallel to Z in Model 1 (Fig. 6) for all strains. Under these conditions, the activity of basal slip increases progressively with increasing strain, and reaches values of more than 50% when $\gamma = 3.5$ ($\varepsilon_{\mathrm{eq}} = 2$) followed by a decrease on the activity of positive and negative rhomb slip

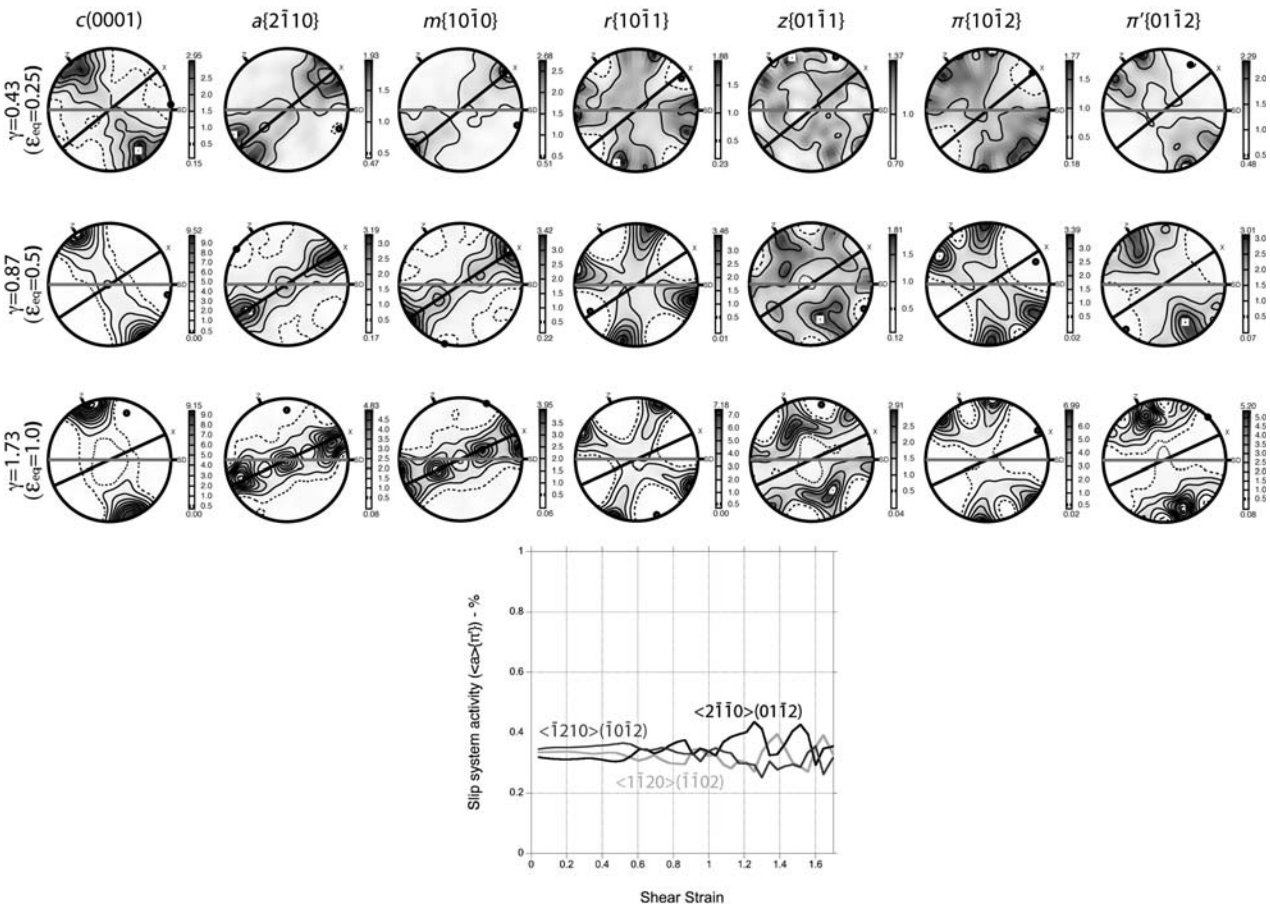

Fig. 5. Lower bound (homogeneous stress) quartz CPO developed in simple shear at equivalent strains ($\varepsilon_{\mathrm{eq}}$) of 0.5, 1.0 and 1.5 (shear strains given as γ) assuming single $\langle a\rangle\{\pi'\}$ slip system. Pole figures are lower hemisphere equal-area projections for 1000 orientations. Maximum and minimum finite strain axes are marked X and Z. The horizontal line is the shear plane, whereas the tilted black line marks the flattening plane. The shear sense is dextral, top to the right and SD is the shear direction. Contours of multiples of uniform distribution; inverse log shadings vary from white (minimum density) to black (maximum density). Slip-system activity for the individual slip systems of the $\langle a\rangle\{\pi'\}$ family is also indicated. Note that at low strains, the activity of individual slip systems does not vary; with increasing strain however, there is always a dominance of one member over the others and a frequent interchange between dominant systems. The maximum concentration in the pole figures is indicated by the white square.

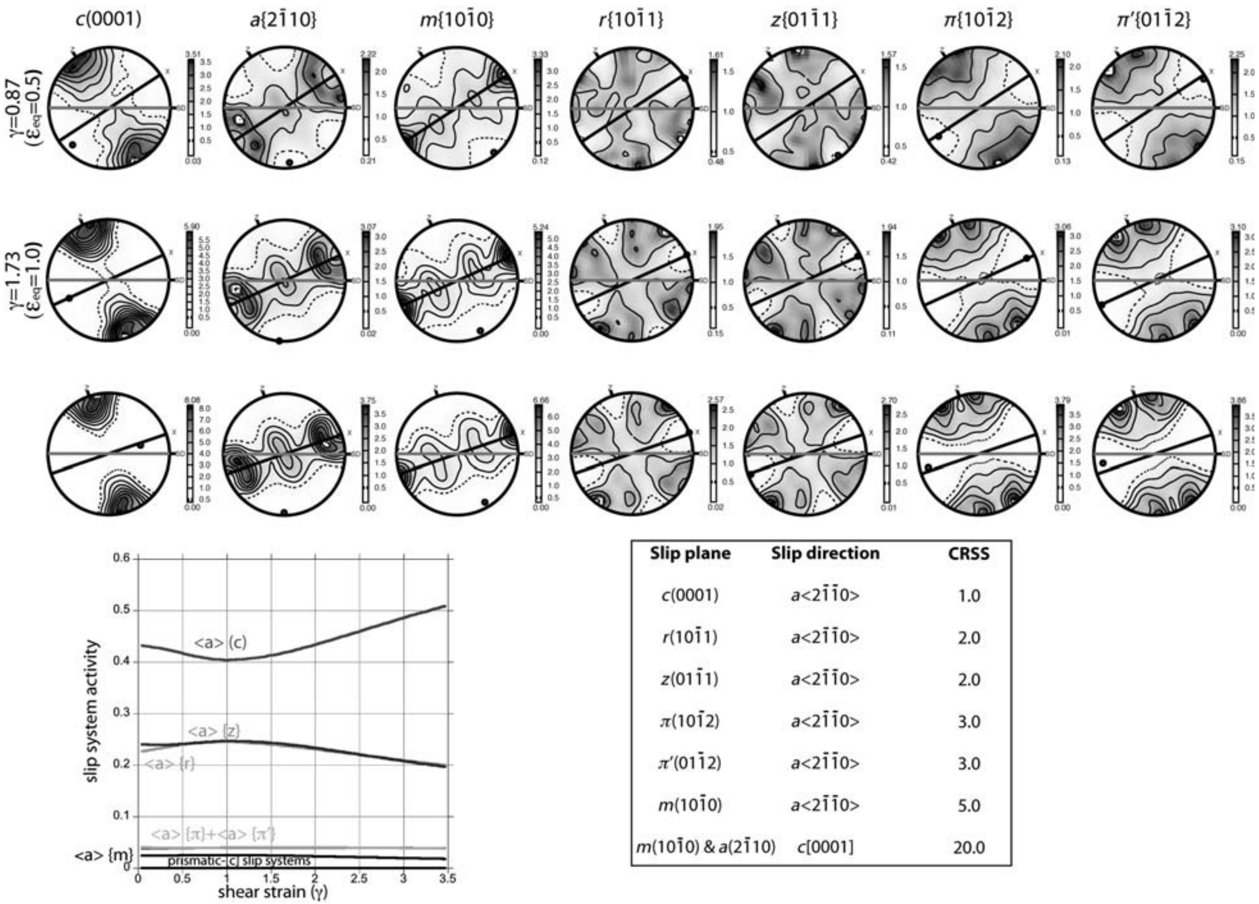

Slip plane	Slip direction	CRSS
$c(0001)$	$a\langle 2\bar{1}\bar{1}0\rangle$	1.0
$r(10\bar{1}1)$	$a\langle 2\bar{1}\bar{1}0\rangle$	2.0
$z(01\bar{1}1)$	$a\langle 2\bar{1}\bar{1}0\rangle$	2.0
$\pi(10\bar{1}2)$	$a\langle 2\bar{1}\bar{1}0\rangle$	3.0
$\pi'(01\bar{1}2)$	$a\langle 2\bar{1}\bar{1}0\rangle$	3.0
$m(10\bar{1}0)$	$a\langle 2\bar{1}\bar{1}0\rangle$	5.0
$m(10\bar{1}0)$ & $a(2\bar{1}10)$	$c[0001]$	20.0

Fig. 6. Quartz CPO developed in simple shear at equivalent strains ($\varepsilon_{\mathrm{eq}}$) of 0.5, 1.0 and 1.5 (shear strains given by γ). Anisotropic VPSC model (Model 1), $\alpha = 1$, ‘normal’ CRSS values for different slip systems of quartz as expected in low-to-intermediate deformation temperatures (see values in the box). Pole figures are plotted in lower hemisphere, equal-area projections for 1000 grains. East–west horizontal line marks the shear plane (SD is the shear direction), whereas the tilted black line marks the finite strain reference frame. Contours are multiples of uniform distribution; inverse log shadings vary from white (minimum density) to black (maximum density). Note the dominance of basal slip in $\langle a\rangle$ direction and its increasing activity with progressive deformation, and how the maximum of [c]-axes remains subparallel to the foliation pole even at relatively high-strain magnitudes. The maximum concentration in the pole figures is indicated by the white square.

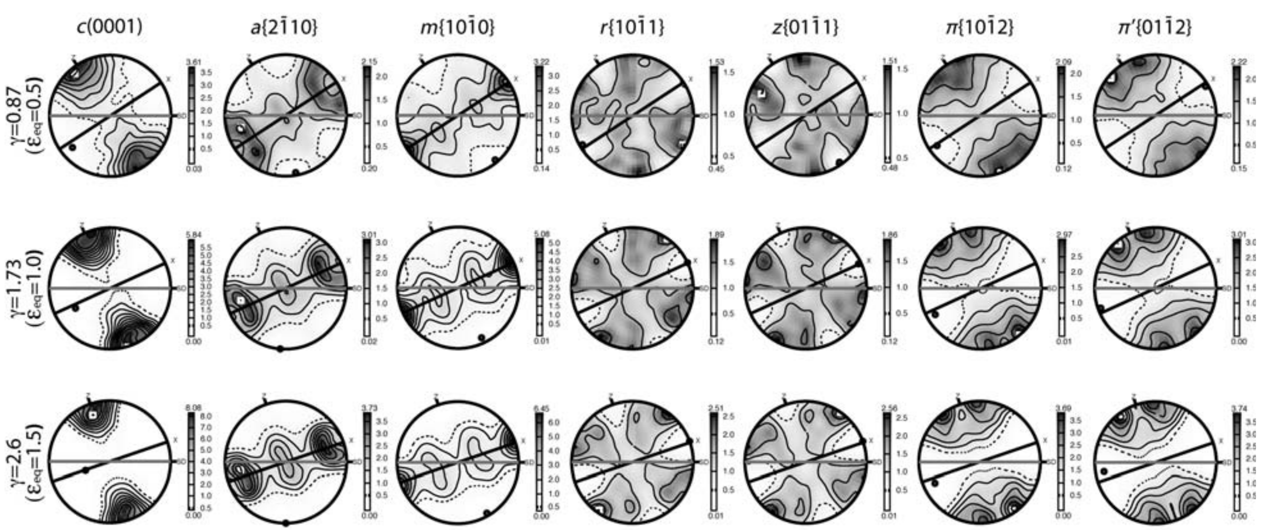

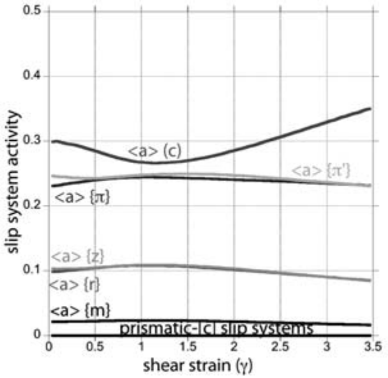

Slip plane	Slip direction	CRSS
c(0001)	a<2$\bar{1}\bar{1}$0>	1.0
r(10$\bar{1}$1)	a<2$\bar{1}\bar{1}$0>	2.5
z(01$\bar{1}$1)	a<2$\bar{1}\bar{1}$0>	2.5
π(10$\bar{1}$2)	a<2$\bar{1}\bar{1}$0>	1.5
π′(01$\bar{1}$2)	a<2$\bar{1}\bar{1}$0>	1.5
m(10$\bar{1}$0)	a<2$\bar{1}\bar{1}$0>	20.0
m(10$\bar{1}$0) & a(2$\bar{1}\bar{1}$0)	c[0001]	20.0

Fig. 7. Quartz CPO developed in simple shear at equivalent strains ($\varepsilon_{\mathrm{eq}}$) of 0.5, 1.0 and 1.5 (shear strains given by γ). Anisotropic VPSC model (Model 2), $\alpha = 1$. The CRSS for basal, acute rhomb and rhomb slip systems in $\langle a \rangle$ direction are approximately the same (the latter two are slightly stronger than the former; see values in the box). Pole figures plotted in lower hemisphere; equal-area projections for 1000 grains. East–west horizontal line marks the shear plane (SD is the shear direction), whereas the tilted black line marks the finite-strain reference frame. Contours are multiples of uniform distribution; inverse log shadings vary from white (minimum density) to black (maximum density). Note that the activity of $\langle a \rangle (c)$ is just slightly higher than the activity of $\langle a \rangle \{\pi\}$ and $\langle a \rangle \{\pi'\}$. Also note the variation of [c]-axes maxima and how the maximum of [c]-axes rotates from Z about W towards Y with increasing strain. The maximum concentration in the pole figures is indicated by the white square.

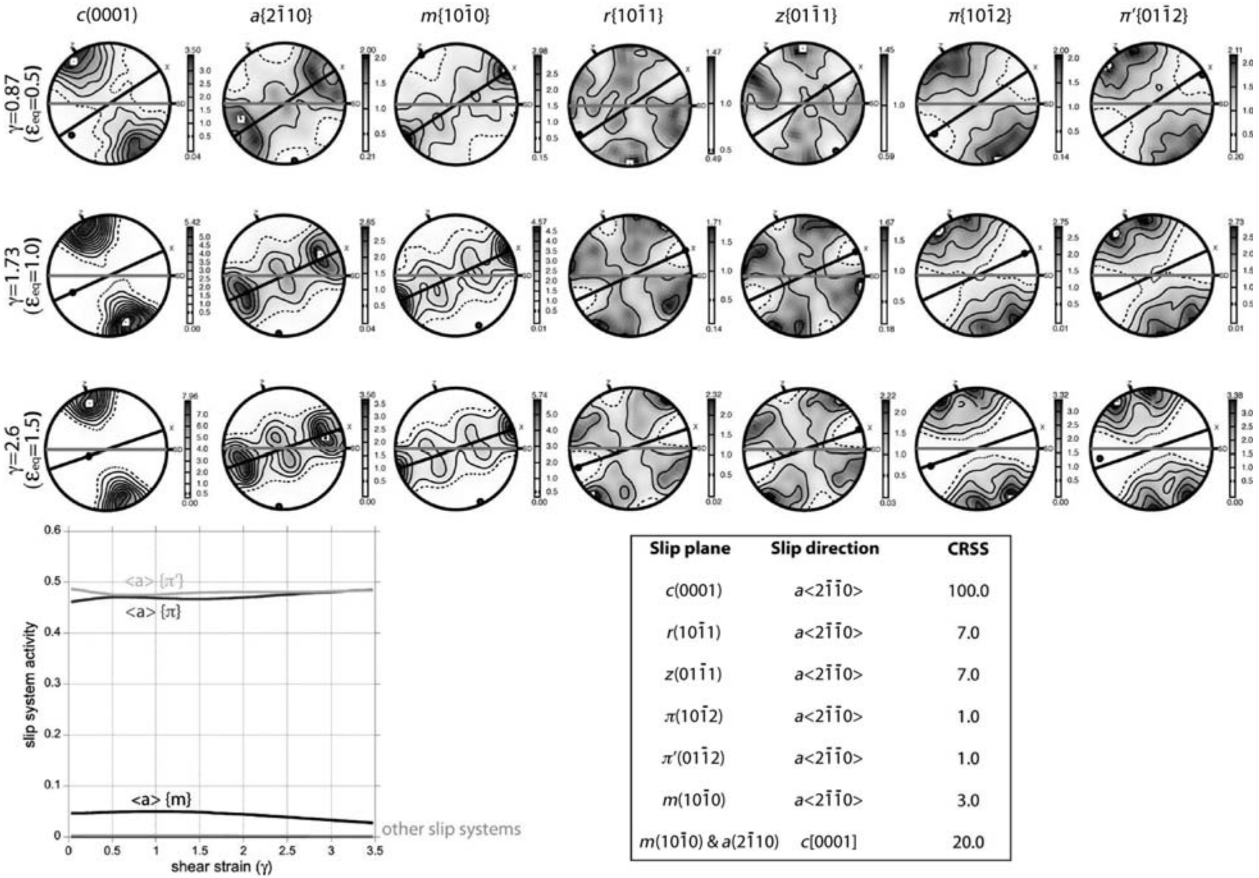

Slip plane	Slip direction	CRSS
c(0001)	a<2$\bar{1}\bar{1}$0>	100.0
r(10$\bar{1}$1)	a<2$\bar{1}\bar{1}$0>	7.0
z(01$\bar{1}$1)	a<2$\bar{1}\bar{1}$0>	7.0
π(10$\bar{1}$2)	a<2$\bar{1}\bar{1}$0>	1.0
π′(01$\bar{1}$2)	a<2$\bar{1}\bar{1}$0>	1.0
m(10$\bar{1}$0)	a<2$\bar{1}\bar{1}$0>	3.0
m(10$\bar{1}$0) & a(2$\bar{1}\bar{1}$0)	c[0001]	20.0

Fig. 8. Quartz CPO developed in simple shear at equivalent strains (ε_{eq}) of 0.5, 1.0 and 1.5 (shear strains given by γ). Anisotropic VPSC model (Model 3), $\alpha = 1$, CRSS for $\langle a\rangle\{\pi'\}$ slip system is much lower than for basal, positive acute and rhomb systems (see values in the box). Pole figures plotted in lower hemisphere; equal-area projections for 1000 grains. East–west horizontal line marks the shear plane (SD is the shear direction), whereas the tilted black line mark the finite strain reference frame. Contours are multiples of uniform distribution; inverse log shadings vary from white (minimum density) to black (maximum density). Note that the predominance activity of $\langle a\rangle\{\pi'\}$ over the other slip systems, following the same behaviour of basal slip activity in Figure 6. In this setup, the maximum concentration of [c]-axes is at a low angle with Z in $\varepsilon_{eq} \leq 1$. The maximum concentration in the pole figures is indicated by the white square.

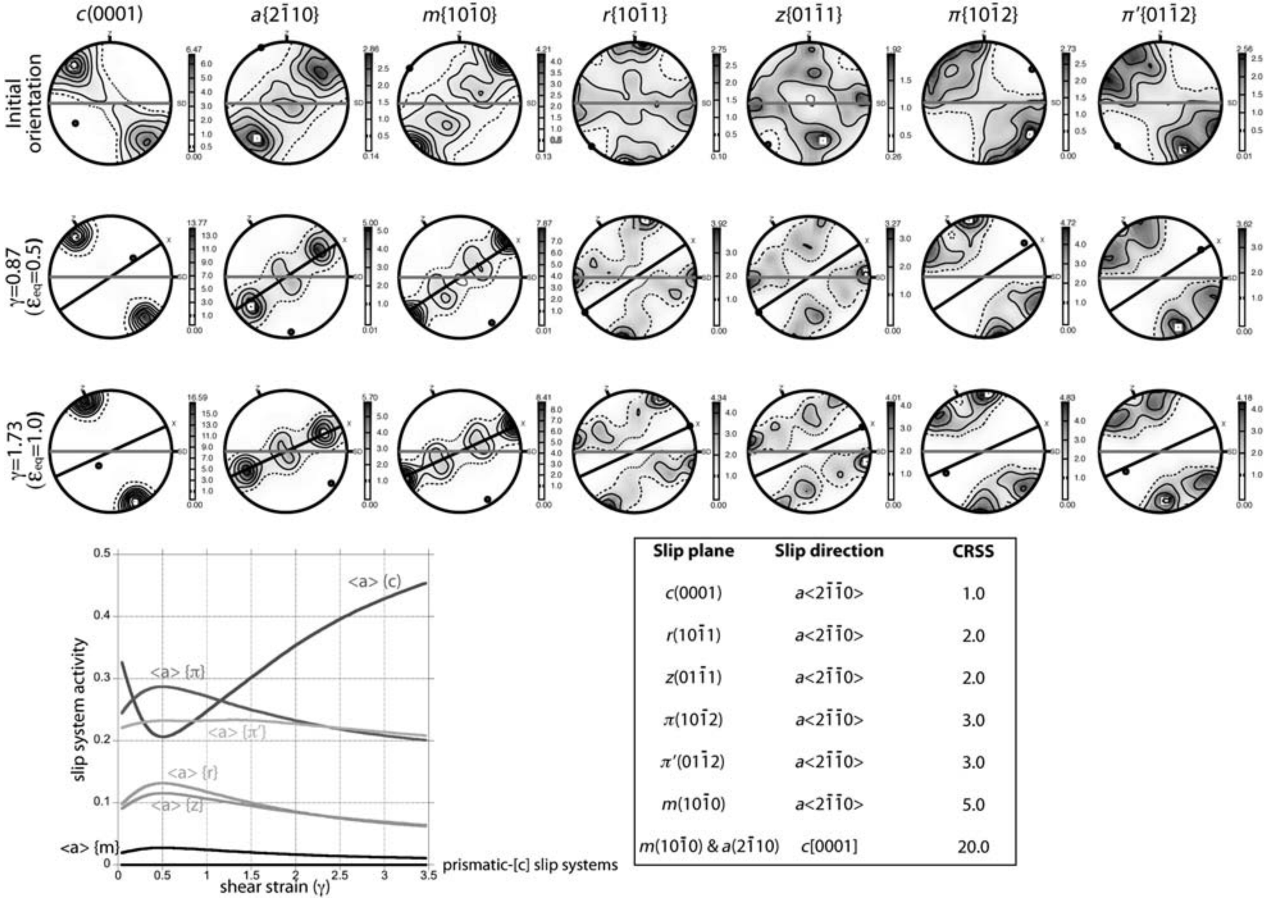

Slip plane	Slip direction	CRSS
c(0001)	*a*<2$\bar{1}\bar{1}$0>	1.0
r(10$\bar{1}$1)	*a*<2$\bar{1}\bar{1}$0>	2.0
z(01$\bar{1}$1)	*a*<2$\bar{1}\bar{1}$0>	2.0
π(10$\bar{1}$2)	*a*<2$\bar{1}\bar{1}$0>	3.0
π'(01$\bar{1}$2)	*a*<2$\bar{1}\bar{1}$0>	3.0
m(10$\bar{1}$0)	*a*<2$\bar{1}\bar{1}$0>	5.0
m(10$\bar{1}$0) & *a*(2$\bar{1}$10)	c[0001]	20.0

Fig. 9. Quartz CPO developed in simple shear at equivalent strains ($\varepsilon_{\mathrm{eq}}$) of 0.5, 1.0 and (shear strains given by γ), starting from a previous orientation. Anisotropic VPSC model (Model 4), $\alpha = 1$, CRSS for different slip systems are the same of Figure 7. Pole figures plotted in lower hemisphere; equal-area projections for 1000 grains. East–west horizontal line marks the shear plane (SD is the shear direction), whereas the tilted black line marks the finite strain reference frame. Contours are multiples of uniform distribution; inverse log shadings vary from white (minimum density) to black (maximum density). Note the abrupt changes in the activities of $\langle a\rangle(c)$, $\langle a\rangle\{\pi'\}$ and $\langle a\rangle\{\pi\}$. In these simulations, the maximum of [c]-axes in the pre-existing orientation moves towards the foliation pole with increase strain and remains in that position even at high-strain magnitudes. The maximum concentration in the pole figures is indicated by the white square.

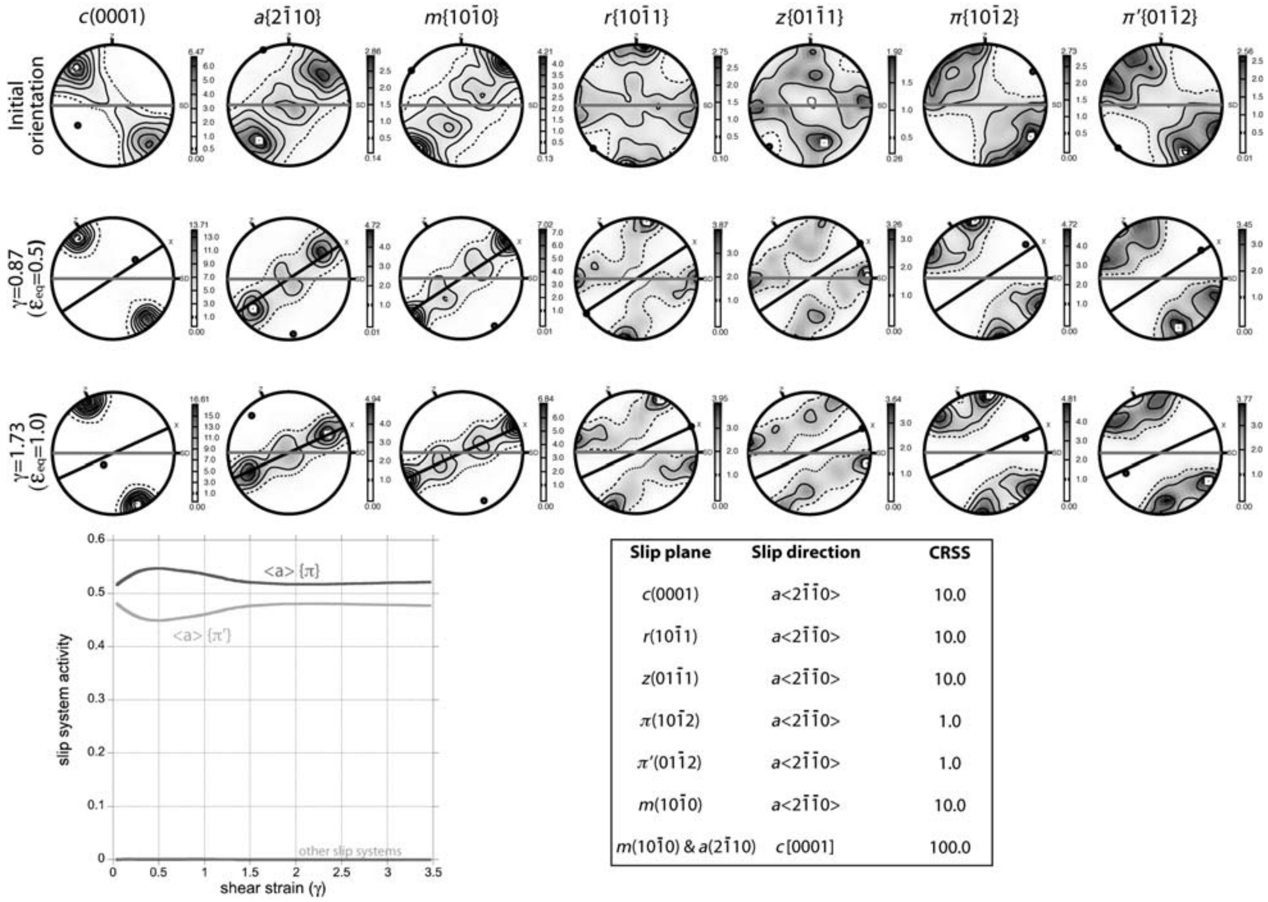

Slip plane	Slip direction	CRSS
c(0001)	a<2$\bar{1}\bar{1}$0>	10.0
r(10$\bar{1}$1)	a<2$\bar{1}\bar{1}$0>	10.0
z(01$\bar{1}$1)	a<2$\bar{1}\bar{1}$0>	10.0
π(10$\bar{1}$2)	a<2$\bar{1}\bar{1}$0>	1.0
π'(01$\bar{1}$2)	a<2$\bar{1}\bar{1}$0>	1.0
m(10$\bar{1}$0)	a<2$\bar{1}\bar{1}$0>	10.0
m(10$\bar{1}$0) & a(2$\bar{1}$10)	c[0001]	100.0

Fig. 10. Quartz CPO developed in simple shear at equivalent strains ($\varepsilon_{\mathrm{eq}}$) of 0.5, 1.0 and (shear strains given by γ), starting from a previous orientation. Anisotropic VPSC model (Model 5), $\alpha = 1$. The CRSS for $\langle a\rangle\{\pi'\}$ is much lower than the values for others slip systems (see values in the box). Pole figures plotted in lower hemisphere; equal-area projections for 1000 grains. East–west horizontal line marks the shear plane (SD is the shear direction), whereas the tilted black line marks the finite strain reference frame. Contours are multiples of uniform distribution; inverse log shadings vary from white (minimum density) to black (maximum density). Although the activity of the negative acute rhomb slip system is dominant, the maxima of [c]-axes is not retained and, with increasing strain, it becomes subparallel to the foliation pole. The maximum concentration in the pole figures is indicated by the white square.

systems (Fig. 6). In Model 2 a similar situation is observed when $\varepsilon_{eq} = 1$; with increasing shear strain, however, the maximum concentration of [*c*]-axes rotates by 18° about *X* from *Z* towards *Y* (Fig. 7). The activity of $\langle a\rangle(c)$ predominates with an average of 30%; the level of activity of $\langle a\rangle\{\pi\}$ and $\langle a\rangle\{\pi'\}$ are similar at around 25%. Again, the activity of $\langle a\rangle(c)$ slip predominates and becomes more important with increasing strain. The maximum concentration of $\{\pi\}/\{\pi'\}$ poles are not exactly parallel to *Z*. They are distributed in double symmetrical maxima at low angles to *Z*, where one of these maxima is normal to the shear plane. The activity of basal slip is nearly zero in Model 3, and the predicted CPO is developed with the dominant activity of the $\langle a\rangle\{\pi\}$ and $\langle a\rangle\{\pi'\}$ slip systems with activities around 47% for each of these systems and with low activities of the $\langle a\rangle\{\mathrm{m}\}$, $\langle a\rangle\{r/z\}$ and $\langle a\rangle(c)$ slip systems. Note that the point maxima of [*c*]-axes is at a small angle to *Z* under relatively low shear strains (Fig. 8). The activity of the positive and negative acute rhomb slip systems does not vary substantially with increasing strain in Model 3. In this model, $\{\pi'\}$ and $\{\pi\}$ poles are at low angles to the foliation pole (*Z*) and oblique to the shear plane (Fig. 8).

The distribution patterns of other important crystallographic directions of quartz are nearly the same in all simulations. The poles of first- $\{m\}$ and second- $\{a\}$ order prisms are distributed along a discontinuous girdle parallel to the foliation, with the maxima oriented either nearly parallel to the shear direction for $\{a\}$ or parallel to the macroscopic lineation (*X*) for $\{m\}$. The poles to $\{r\}$ and $\{z\}$ rhombs occur in four maxima at 55° to the *Z*-axis. The poles of acute rhombs $\{\pi\}$ and $\{\pi'\}$ are distributed in conical girdles around *Z*, also developing four symmetrical point-maxima with similar pole concentrations. The maximum concentration in these pole figures also lies in the *XZ* plane, making an angle of 20° with *Z*. In contrast to Taylor–Bishop–Hill simulations for progressive bulk simple shear (Lister & Hobbs 1980), VPSC simulations indicate a symmetrical relationship between crystal fabrics and finite strain axes regardless of the imposed bulk shear strain (Figs 5–8).

VPSC simulations starting from a previous CPO

Two models were tested. The first used the same set of CRSS values used in Model 2 (Model 4; Fig. 9). The second used a low CRSS of 1.0 for $\langle a\rangle\{\pi/\pi'\}$ slip systems with a CRSS of 100.0 for $[c]\{a\}$ and $[c]\{m\}$ slip systems and a CRSS of 10 for all other slip systems (Model 5; Fig. 10). The CPOs are nearly the same as those predicted from an initial random orientation, and the only qualitative difference is the CPO strength which is much stronger than those modelled in Figures 6–8. In addition, only relatively small shear strains ($\gamma < 0.87$) are necessary to bring the quartz crystallographic axes from their initial tilted position to a position nearly parallel to the finite strain axes used as the reference frame for the pole figures (Figs 9 & 10). Quartz [*c*]-axes are distributed in a single maximum subparallel to the foliation pole *Z* and oblique to the imposed shear plane. The initial *c*-axis maximum rotates in the direction of applied shear strain (dextral: top to the right) towards *Z*, while the *a* and *m* poles simultaneously rotate towards the *XY* plane. The poles to $\{a\}$ and $\{m\}$ are distributed in a continuous girdle nearly parallel to the *XY* plane but inclined in relation to the shear plane, with maximum concentrations within the foliation at about 20° from *X* and parallel to *X*. The poles to rhomb and acute rhombs are distributed as complete or incomplete small circle (conical) girdles centred around *Z*, and the predicted CPOs are no stronger than the CPOs presented for Models 1–3 in Figures 6–8.

In terms of activity, however, the models differ significantly and the relative activities of different slip systems in the models vary in magnitude. In Model 4 presented in Figure 9, the initial decrease of activity of $\langle a\rangle(c)$ up to a shear stain of 0.5 and then its progressive increase with increasing imposed shear strain (reaching values of 45%) is much more accentuated than in Model 2 (Fig. 7). A reciprocal behaviour (increasing and decreasing activity with strain) is seen for all the other important slip systems (Fig. 9) and the activity of $\langle a\rangle\{\pi\}$ and $\langle a\rangle\{\pi'\}$ is (on average) 25%. When $\langle a\rangle\{\pi/\pi'\}$ are the dominant slip systems (Fig. 10), there are no strong variations in their activities (around 50% for each) and a small decrease in the activity of one is compensated for by a small increase in the activity of the other.

Discussion

TEM observations

The microstructures observed by transmission electron microscopy indicate that dislocation glide was an important deformation mechanism in the mature Torridon mylonite, as documented by the high dislocation density in a number of grains (Fig. 4c, d) which confirmed the intense plastic deformation of this rock (Law *et al.* 1990; Lloyd *et al.* 1992). Some of the crystals exhibit an alignment of dislocations, suggesting that some of the dislocation lines have a strong crystallographic control. Other dislocation lines appear curved (Fig. 4d) however, which may result from dislocation pinning by crystal impurities or by the interference between dislocation lines in different planes (e.g. Poirier 1985). Geometrical analysis of dislocations using different diffraction vectors in the same crystal indicate that dislocation glide occurs in the $\{\pi'\}$ and $\{z\}$ slip planes in the $\langle a\rangle$ direction (Figs 2 & 3). The presence of hexagonal arrays of screw $\langle a\rangle$-type dislocations (Fig. 4e, f) in the basal plane suggests that climb was active as these dislocation nodes can no longer glide. It is possible that the $\langle a\rangle(c)$ slip system was active in accommodating deformation, but no direct evidence is provided by our TEM observations of the dislocation networks as the $\langle a\rangle$ screw dislocations could have cross-slipped from other planes (Fig. 4e, f).

Taken together, the activation of these three slip systems confirms the importance of dislocation glide in the development of the strong quartz CPO in the mature mylonite shown in Figure 1 (Law *et al.* 1990; Lloyd *et al.* 1992; Lloyd 2004). In addition, these honeycomb-type dislocation networks and the presence of elongate subgrains also suggest the activation of significant dislocation climb, which is an efficient mechanism for allowing continuous dislocation propagation (Nicolas & Poirier 1976; Poirier 1985; McLaren 1991; Mainprice & Jaoul 2009). During glide-controlled deformation, dislocations in the basal plane may have three different coplanar Burgers' vectors, $[a_1]$, $[a_2]$ and $[a_3]$, which lie at 120° to each other due to the symmetry of quartz. These dislocations probably started to move independently but, once they intersected to form triple junctions, they form sessile junctions and dislocation glide stops.

For continuous deformation and to avoid strain hardening, dislocations have to climb from their original planes to other crystallographic planes (a process driven by diffusion) where they interact with the dislocations present on these planes (e.g. Poirier 1985; Trepmann & Stöckhert 2003). Despite the small direct impact of dislocation climb for the CPO development, it allows dislocation glide in a given plane to continue, which directly favours the development of strong preferred orientation related to a specific slip system. On the other hand, as suggested by the contrast variation observed in Figure 4c, d, crystal bending is insignificant both in terms of strain accommodation and CPO development but it does maintain local strain continuity in the sample and may have some importance during early stages of deformation. Glide-related recovery and heterogeneous deformation are documented by the presence of a variety of subgrain boundaries with a single family of dislocations forming tilt walls (Fig. 4a) and more complex boundaries composed of several families of dislocations (Fig. 4e, f). These subgrains are then subdivided into smaller subgrains, suggesting a process of creep polygonization (e.g. Poirier 1985). On the other hand, grain-boundary migration recrystallization is limited to a few bulging microstructures (Fig. 4d) and, in this case, does not contribute significantly to CPO development or recovery process. The optically detected grain sizes observed in the S_A foliation (Law *et al.* 1990, fig. 2c) and those observed in the TEM images are essentially the same; this implies that, despite the strong preferred orientation, quartz crystals are easily individualized and their boundaries not masked by rotation of the polarizing stage of the optical microscope (in contrast to what was reported by Trepmann & Stöckhert (2003) in other quartz-rich mylonites).

VPSC modelling

The characteristic features of the mature Torridon mylonite (Fig. 1) CPO are: (1) the $[c]$-axes form a strong maxima near the pole of the shear-zone margin and oblique to foliation in the mature mylonite; (2) the $\{a\}$ and $\{m\}$ poles form girdles parallel to the shear-zone margin reference plane; (3) the $\{r\}$ and $\{z\}$ poles are positioned on conical surfaces of large opening angle centred about the pole of the shear-zone margin; and (4) the $\{\pi\}$ and π' poles are oriented on conical surfaces of lower opening angle centred about Z. Most of the CPO features of the mature mylonite can be reproduced by homogeneous simple-shear VPSC modelling using two different approaches (Models 2 and 3; Figs 7 & 8), but cannot be reproduced in Model 1 where $\langle a\rangle$ (c) dominates the slip activity and forms a CPO with a strong c-axis maxima parallel to Z at all strains. A similar situation is observed in Model 2 but, at equivalent strains >1, the maximum concentration of $[c]$-axes rotates from Z toward Y around X and becomes parallel to the $[c]$-axis maxima observed in the mature mylonite (Figs 1 & 7). The activity of basal slip dominates and becomes more important with increasing strain, but the difference between the activities of $\langle a\rangle\{\pi\}$ and $\langle a\rangle\{\pi'\}$ is small. For Model 2 (Fig. 7), the critical resolved shear stress of the $\langle a\rangle\{\pi\}$ and $\langle a\rangle\{\pi'\}$ slip systems are slightly stronger at 1.5 than the resolved shear stress for the $\langle a\rangle(c)$ system at 1.0. In addition, the CRSS of positive and negative rhomb slip systems at 2.5 are higher than the value for the acute rhomb systems; otherwise, the maximum concentration of $[c]$-axes would become parallel to Z direction as in Model 1 or at higher angles toward Y (Fig. 6). In Model 3 on the other hand, the maximum concentration of $[c]$-axes near Z in the YZ plane develops at low strains ($\varepsilon_{eq} \leq 1$). The acute rhomb slip systems $\langle a\rangle\{\pi/\pi'\}$ in this model have a low CRSS of 1.0 plus a CRSS of 3.0 for $\langle a\rangle\{m\}$ and a CRSS value higher than 7.0 for all other slip systems (Fig. 8). Model 3 results in the slip activity being dominated by $\langle a\rangle\{\pi/\pi'\}$, with small activity of $\langle a\rangle\{m\}$.

The critical resolved shear stress for different slip systems of quartz depends on a number of physical parameters (e.g. temperature, stress/strain rate, presence of water) and, as shown by our models, qualitatively the CPO patterns are essentially the same (Figs 6–8). Nevertheless, small variations of the CRSS may lead to slight but important modifications in positions of the maximum concentration of the quartz crystallographic axes. For example, a decrease in the CRSS for the $\langle a\rangle\{\pi\}$ and $\langle a\rangle\{\pi'\}$ by half of its original value of 3.0 (considering the expected active slip systems at low-to-medium deformation temperatures for quartz; Fig. 6) induces a change in the [*c*]-axes maxima orientation from parallel to *Z* to an intermediary position at *c*. 18° from *Z* in the *YZ* plane under high-strain conditions (Fig. 7). On the other hand, a ten-fold increase of the $\langle a\rangle(c)$ CRSS and a seven-fold increase in the $\langle a\rangle\{r\}$ and $\langle a\rangle\{z\}$ CRSS are necessary to produce a similar concentration under lower strain conditions, with no significant variations in the general CPO patterns (Fig. 8).

In the simulated aggregates with initial crystallographic preferred orientation, the CPO becomes very strong at relatively low shear strains when compared to models with initial random orientations. The initial [*c*]-axis maximum is rotated to an intermediate position between the starting orientation and the pole to foliation *Z*. The activity of different slip systems has more accentuated increases and decreases than the simulations starting from a random orientation. One explanation for rapid rotation as a function of finite strain is that the starting orientations for the simulations with an inherited fabric have a relatively high number of orientations in geometrically favourable positions for slip compared to a random fabric. As an example, the activity of $\{\pi\}$, $\{\pi'\}$, $\{r\}$, $\{z\}$ and $\{m\}$ in a common $\langle a\rangle$ slip direction increases initially because the initial orientation, with the [*c*]-axis maxima aligned with the shear direction, favours the slip on these planes, even if their CRSSs are assumed to be higher than for $\langle a\rangle(c)$ (Fig. 9). Slip on the (*c*)-planes is not initially favoured as it is oriented 90° from the slip direction. Note that slip does not occur in the [*c*]-direction, although this direction is at a low angle to the shear direction, because the resolved shear stress is assumed to be high (>20.0). When rotation proceeds and the general orientation of the basal planes becomes aligned closer to the finite strain flattening plane, basal slip is favoured again. Its activity increases substantially, inducing the progressive rotation from the original maxima direction towards the direction *Z*. In Model 5, where $\langle a\rangle\{\pi\}$ and $\langle a\rangle\{\pi'\}$ are the only easy slip systems with CRSS of 1.0 and even $\langle a\rangle(c)$ is difficult, then the only slip planes that contribute significantly to slip activity are $\{\pi\}$ and $\{\pi'\}$. The sum of their activities reaches values around 100%, and the activities of the other slip systems are virtually negligible. The $\{r\}$ planes are initially about 45° from the shear direction which explains why $\langle a\rangle\{r\}$ is favourably oriented for slip at low strain, but once the rotation starts the $\{\pi'\}$ planes become more favourably oriented and dominate the slip activity.

In summary, crystal preferred orientations predicted via VPSC modelling evolve continuously with strain, showing strong CPOs of quartz for shear strains ≥ 2, in a similar way to olivine fabrics using the same type of numerical modelling (Tommasi *et al.* 2000). Fabric strength indicated by the *J*-index (Bunge 1982) reaches values of around 14 and 25 for $\gamma = 3.5$ in simulations starting from random and non-random orientations, respectively. On the other hand the Torridon quartz mylonite, which has an anomalously strong preferred orientation, has a *J* value of 8.6 (Fig. 11). The shear strain estimations based on the inflection of foliation into the shear zone (Ramsay 1967) gives values of $\gamma > 5$ (Lloyd *et al.* 1992) or $\gamma \sim 8$ at the shear-zone centre, when we consider the minimum angle of 9° between the mylonitic foliation (finite strain flattening plane) and the vein margins (shear plane).

In our models, the calculated *J*-indices for the above variation in shear strain, based on the geometrical relationships between shear direction and the *X* finite strain axis, gives values from 17–25 in the models with initial random orientation and 23–30 in the models with an initial crystal orientation (Fig. 11). When plotted on the modelled curves, the *J*-index of the mature mylonite indicates a γ of *c*. 2 which represents an angle of *c*. 36° between the shear direction and the *X*-axis. This indicates that the VPSC modelling underestimates the shear strain necessary to generate a CPO with the same *J*-index value as determined in the natural mylonite. On the other hand, the *J*-indexes calculated from our models are clearly overestimated when compared to the value of the natural sample. In both cases, this may be explained by the fact that VPSC models only take into account deformation by dislocation glide. Mechanisms such as dynamic recrystallization that in nature and experiments may cause crystal orientation dispersion (e.g. Karato 1988; Trimby *et al.* 1998; Fliervoet *et al.* 1999; Barnhoorn *et al.* 2004) are not considered in these models.

Dislocation glide and the development of crystal preferred orientation, as simulated by viscoplastic self-consistent modelling, therefore has to be assisted by other material processes to accommodate deformation effectively in natural rocks. Due the pervasive presence of subgrains at different

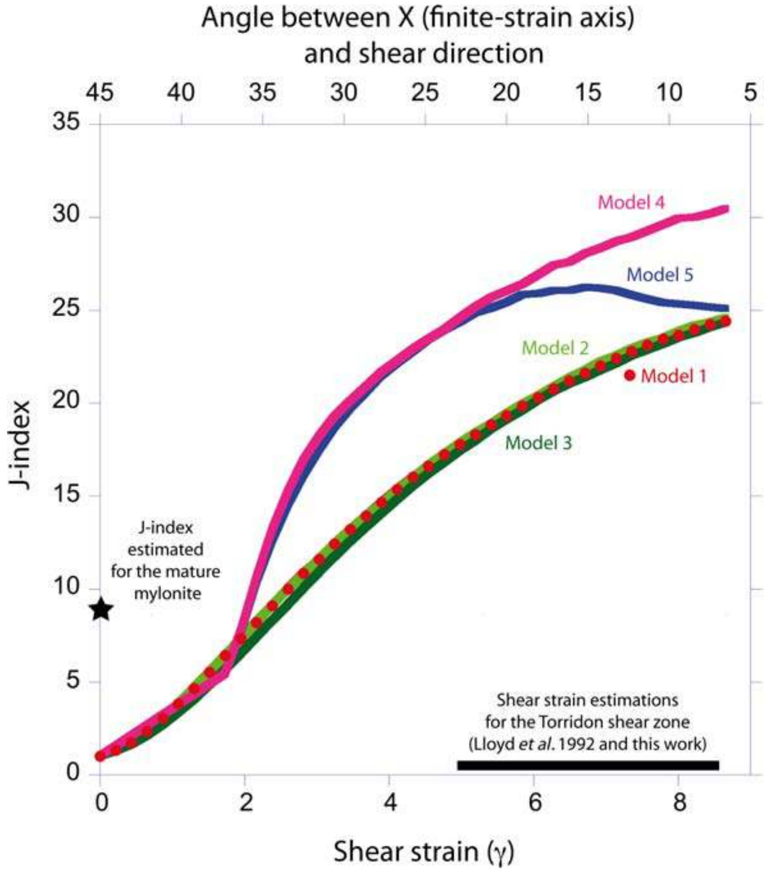

Fig. 11. Evolution of the CPO strength represented by the *J*-index (i.e. the integral of the square of orientation distribution function; Bunge 1982) as a function of the shear strain for the anisotropic VPSC models presented in Figures 6–10. The black star on the *Y*-axis indicates the *J*-index of the mature Torridon mylonite. The respective curves for each model are marked directly on the figure. Note a drop in the *J*-index of Model 5 due to the lack of mathematical convergence during modelling.

scales in the Torridon mylonite, in addition to a misorientation angle peak at 15° (Lloyd 2004), this suggests that subgrain rotation recrystallization was the dominant recovery mechanism, aided by grain-boundary migration.

Implications for the Torridon Shear Zone

In comparison with quartz mylonites developed in low- to medium-grade shear zones, the quartz preferred orientations observed in the mature Torridon mylonite present an anomalous maxima of [*c*]-axes at a low angle to the pole to the shear plane, suggesting that the dominant slip system was $\langle a\rangle\{\pi/\pi'\}$. Nevertheless, a predominance of basal slip is to be expected under these conditions followed by rhomb slip and small amounts of prismatic slip, all of them sharing a common $\langle a\rangle$ slip direction (e.g. Fig. 6) where the acute rhomb slip systems are usually of secondary importance (Stipp *et al.* 2002). The differences between the CPO patterns expected in low- to intermediate-temperature quartz mylonites, and what is observed in the Torridon vein, lead us to two possible explanations for the strong concentrations of [*c*]-axes near the *Z* direction but slightly off the periphery of the pole figure. Analysis of potential slip-system orientations for different positions on the quartz [*c*]-axis fabric skeleton, in relation to the shear-zone geometry, indicate that the positive and negative acute rhomb slip systems are strongly aligned with the inferred simple-shear kinematic framework (Law *et al.* 1990). This strong alignment can be interpreted as evidence for the dominant activity of acute rhomb slip in the $\langle a\rangle$ direction, although $\langle a\rangle(c)$ and $\langle a\rangle\{z\}$ slip systems are also operative (Law *et al.* 1990,

p. 43). The CPO supports the bulk simple-shear kinematic framework indicated by the shear-zone geometry. On the other hand, as stated in Lloyd *et al.* (1992), the CPO patterns as a whole can be interpreted as resulting from the operation of multiple slip systems in a common $\langle a\rangle$ slip direction. In addition, the mylonitic fabric of the mature Torridon mylonite was developed in a specific location within the sheared quartz vein/shear zone at a particular shear strain, and essentially depends upon the inherited CPO of the starting material (14 large quartz grains) at that specific location.

Geometrical characterization of dislocations through TEM images demonstrates that $\langle a\rangle\{\pi'\}$ and $\langle a\rangle\{z\}$ were the main slip systems active during flow in the mature mylonite (Figs 2 & 3), possibly together with $\langle a\rangle(c)$ slip (Fig. 4e, f). However, there is a lack of evidence for dislocations on prismatic planes $\{a\}$ and $\{m\}$. The VPSC models in which $\langle a\rangle\{\pi\}$ and $\langle a\rangle\{\pi'\}$ are dominant therefore seem to be physically unrealistic, given the strong activity of $\langle a\rangle\{z\}$ and possibly $\langle a\rangle(c)$ slip systems and given the thermal conditions of shear-zone development (Figs 8 & 10). On the other hand, the CPO predicted under higher shear strains (Fig. 7), where the CRSS for basal slip is slightly lower than for the acute rhomb and rhomb slip systems, is in agreement with the high relative shear strain determined by Lloyd *et al.* (1992) and the TEM observations described in the present paper.

Although Dauphiné twinning is not directly considered in our models and was not observed in TEM analyses, it plays an import role in deformation of the mature Torridon mylonite. In the early stages of deformation, it has an important influence both on grain-size reduction and on the development and maintenance of fine-grained mylonitic structure (Lloyd *et al.* 1992; Lloyd 2004). Due the rotation of 60° around the [c]-axis, Dauphiné twinning causes an increase in the number of symmetrically equivalent $\langle a\rangle\{\pi/\pi'\}$ slip systems. If these slip systems are favourably orientated for slip, their activity can be stronger than the activity of basal slip in the $\langle a\rangle$ direction (e.g. Menegon *et al.* 2010). If the number of symmetrically equivalent $\{\pi/\pi'\}$ planes in favourable orientations for slip due to Dauphiné twinning increases, they may play an important role on the final [c]-axis pattern; this is characterized by a strong maximum close to the pole of the foliation but slightly off the periphery of the pole figures. This is consistent with the observations of Law *et al.* (1990), Lloyd *et al.* (1992) and Lloyd (2004) for the CPO of the mature Torridon mylonite, and is corroborated by our numerical modelling. In addition, as Dauphiné twinning causes an interchange between positive and negative crystallographic forms, it results in the interchange between $\langle +a\rangle$ and $\langle -a\rangle$ slip directions and consequently plays a role in determining whether the crystal is in a favourable position to slip by activation of crystal slip systems in the $\langle a\rangle$ direction.

The ubiquitous presence of subgrains in the mature mylonite as observed in the TEM images, and in the distinct peak of low misorientation angles (<15°) presented by Lloyd (2004), suggests that dynamic recrystallization by subgrain rotation-assisted dislocation creep was dominant during formation of the mature mylonite. Subgrain rotation implies the subdivision of larger-strained crystals into new grains displaying misorientation angles <15° by progressive incorporation of dislocations along subgrain boundaries (e.g. Poirier & Nicolas 1975; White 1979). This process is therefore capable of dispersing the preferred orientation and compensates the increasing CPO strength induced by dislocation glide, allowing the development of a stable orientation. Nevertheless, the scattering of the CPO by rotation recrystallization is relatively weak, and some degree of host control between parent grain and new grains is normally observed (e.g. Poirier 1985; Law *et al.* 1986; Lloyd *et al.* 1992; Lloyd & Freeman 1994). An inherited fabric, such as that observed in the original vein material preserved at the margins of the Torridon quartz vein/shear zone, may therefore be retained even in the case of a strong superimposed deformation as observed in the mature mylonite.

Conclusions

We have applied transmission electron microscopy (TEM) and viscoplastic self-consistent (VPSC) modelling to better constrain the origin of CPO and microstructural development in the Torridon quartz mylonite previously studied by Law *et al.* (1990), Lloyd *et al.* (1992) and Lloyd (2004). TEM analyses showed evidence for $\langle a\rangle\{\pi'\}$ and $\langle a\rangle\{z\}$ slip systems in quartz, and possible activity on $\langle a\rangle(c)$, but no direct evidence for activation of $\langle a\rangle\{m\}$, $[c]\{m\}$ or $[c]\{a\}$ slip systems. There is significant TEM-based evidence for climb-induced recovery in this material, including the presence of hexagonal dislocation networks in the basal plane and subgrain boundaries.

Several models for CPO development using variations in critical resolved shear stress for different slip systems of quartz were investigated with the VPSC modelling approach and, unlike previous models, we have not used the relatively ‘hard’ $\langle c+a\rangle$ slip direction in our simulations. Three models using a standard initial random orientation are presented, and the CPOs generated by these models demonstrate many common characteristics. These include: (1) the high [c]-axis concentration near the finite shorting direction Z; (2)$\{a\}$ and

$\{m\}$ poles distributed in the XY flattening plane; (3) $\{r\}$ and $\{z\}$ poles distributed along conical girdles with large opening angles centred around Z; and (4) $\{\pi\}$ and $\{\pi'\}$ poles also in conical girdles but with small opening angles centred about Z. Many of these features are shared with the mature Torridon mylonite sample. In detail, however, each model has slightly different choices of critical resolved shear stresses for different slip systems of quartz. The different assumed CRSS values lead to slight (but important) modifications in the orientation of the maximum concentration of quartz $[c]$-axes. Model 1 has high activities of $\langle a\rangle(c)$, $\langle a\rangle\{r\}$ and $\langle a\rangle\{z\}$, but only Models 2 and 3 reproduce the c-axis concentration at an angle of *c*. 18° with Z in the YZ plane and a high concentration of $\{\pi'\}$ poles near Z. Model 2 has high $\langle a\rangle(c)$ and $\langle a\rangle\{\pi/\pi'\}$ slip activity. Model 3 has high a dominant $\langle a\rangle\{\pi/\pi'\}$ slip activity, but no basal slip in $\langle a\rangle$.

The models that start with a previous crystal orientation develop a very strong CPO after relatively small strains, following a rapid rotation of the original fabric. This is explained by the fact that the initial non-random fabric has a number of orientations that are geometrically favoured for slip on certain slip systems, for example, favoured slip in $\langle a\rangle\{\pi/\pi'\}$ rather than $\langle a\rangle(c)$ as similarly demonstrated by Pennacchioni *et al.* (2010). Nevertheless, when the rotation proceeds and the basal planes of quartz become aligned with the finite strain plane XY, slip on $\langle a\rangle(c)$ is favoured again and explains why the maximum concentration of quartz $[c]$-axes at a low angle with Z is not retained in these simulations.

Taking into account that recrystallization is not considered in our numerical models but is widely observed in nature (Lloyd *et al.* 1992; Lloyd 2004; Pennacchioni *et al.* 2010), we conclude that initial CPOs can be retained even in the case of strong superimposed deformation. The mutual activation of $\langle a\rangle\{\pi'\}$, $\langle a\rangle\{z\}$ and possibly $\langle a\rangle(c)$ slip systems suggest that the more realistic VPSC model for the CPO development is the one where all of the above slip systems have assumed similar CRSS values (Model 2; Fig. 7). In this situation, the maximum of quartz $[c]$-axes at a low angle to the foliation pole (Z) develops under higher-strain conditions and becomes stable in this position.

We would like to dedicate this paper to the memory of M. Casey, who sadly passed away on 10th June 2008. Martin was much more than a colleague; he was a great friend, a font of inspiration and a tutor, always ready to discuss geological and non-geological problems. We are not sure if he would agree with the conclusions of our paper, but he would undoubtedly have a number of 'simple' questions that would result in very fruitful discussions. The authors are grateful to L. Menegon and an anonymous reviewer for the thoughtful reviews carried out in less than a month, and to D. Prior for all the editorial work (including an unexpected 'second version' of the manuscript). LFGM is particularly grateful to L. Menegon for the copies of two 'in press' papers and all the discussion during the EURISPET in Zürich. LFGM is also grateful to A. Tommasi for advice on VPSC modelling and her encouraging comments about our modelling, and to French Agence Nationale de la Recherche (ANR) for a post-doctoral fellowship (Project Crystaltex). We also thank R. Marshall (University of Leeds) for specimen preparation. The automated EBSD system was funded by UK NERC Grant GR9/3223 (GEL).

References

BAËTA, R. D. & ASHBEE, K. H. G. 1969. Slip systems in quartz, II: interpretation. *American Mineralogist*, **54**, 1574–1582.

BARNHOORN, A., BYSTRICKY, M., BURLINI, L. & KUNZE, K. 2004. The role of recrystallisation on the deformation behaviour of calcite rocks: large strain torsion experiments on Carrara marble. *Journal of Structural Geology*, **24**, 885–903.

BOULLIER, A. M. & GUEGUEN, Y. 1975. S.-P mylonites. Origin of some mylonites by superplastic flow. *Contributions to Mineralogy and Petrology*, **50**, 121–134.

BUNGE, H.-J. 1982. *Texture Analysis in Materials Science*. Butterworths, London.

CANOVA, G. R., WENK, H.-R. & MOLINARI, A. 1992. Simulation of texture development in polyphase materials. *Acta Metallurgica et Materalia*, **40**, 1519–1530.

CARTER, N. L. & TSENN, C. 1987. Flow properties of continental lithosphere. *Tectonophysics*, **136**, 27–63.

CASEY, M. & MCGREW, A. J. 1999. One-dimensional kinematic model of preferred orientation development. *Tectonophysics*, **303**, 131–140.

CHASTEL, Y. B., DAWSON, P. R., WENK, H.-R. & BENNET, K. 1993. Anisotropic convection with implications for the upper mantle. *Journal of Geophysical Research*, **98**, 17 757–17 771.

DIXON, J. & WILLIAMS, G. 1983. Reaction softening in mylonites from the Arnaboll thrust Sutherland. *Scottish Journal of Geology*, **19**, 157–168.

ESHELBY, J. D. 1957. The determination of the elastic field of an ellipsoidal inclusion, and related problems. *Proceedings of the Royal Society of London, Series A*, **241**, 376–396.

ETCHECOPAR, A. 1977. A plane kinematic model of progressive deformation in a polycrystalline aggregate. *Tectonophysics*, **39**, 121–139.

FITZ GERALD, J. D. & STÜNITZ, H. 1993. Deformation of granitoids at low metamorphic grade I: reactions and grain size reduction. *Tectonophysics*, **221**, 269–297.

FITZ GERALD, J. D., MANCKTELOW, N. S., PENNACCHIONI, G. & KUNZE, K. 2006. Ultra-fine grained quartz mylonites from high-grade shear zones: evidence for a strong dry mid-to-lower crust. *Geology*, **34**, 369–372.

FLIERVOET, T. F., DRURY, M. R. & CHOPRA, P. N. 1999. Crystallographic preferred orientations and misorientations in some olivine rocks deformed by diffusion or dislocation creep. *Tectonophysics*, **303**, 1–27.

FRONDEL, C. 1962. *The System of Mineralogy, vol III – Silica Minerals*. 7th edn. Wiley, New York.

GLEASON, G. C., TULLIS, J. & HEIDELBACH, F. 1993. The role of dynamic recrystallization in the development of lattice preferred orientations in experimentally deformed quartz aggregates. *Journal of Structural Geology*, **15**, 1145–1168.

GOODWIN, L. B. & WENK, H.-R. 1995. Development of phyllonite from granodiorite – mechanisms of grain-size reduction in the Santa Rosa mylonite zone, California. *Journal of Structural Geology*, **17**, 689–707.

GRIGGS, D. T. & BLACIC, J. D. 1965. Quartz: anomalous weakness of synthetic crystals. *Science*, **147**, 292–295.

HALFPENNY, A., PRIOR, D. J. & WHEELER, J. 2006. Analysis of dynamic recrystallization and nucleation in a quartzite mylonite. *Tectonophysics*, **427**, 3–14.

HEILBRONNER, R. & TULLIS, J. 2002. The effect of static annealing on microstructures and crystallographic preferred orientations of quartzites experimentally deformed in axial compression and shear. *In*: DE MEER, S., DRURY, M. R., DE BRESSER, J. H. P & PENNOCK, G. M. (eds) *Deformation Mechanisms, Rheology and Tectonics: Current Status and Future Perspectives*. Geological Society, London, Special Publications, **200**, 191–218.

HEILBRONNER, R. & TULLIS, J. 2006. Evolution of *c*-axis pole figures and grain size during dynamic recrystallization: results from experimentally sheared quartzite. *Journal of Geophysical Research*, **111**, B10202, doi: 10.1029/2005JB004194.

HIPPERTT, J. F. 1998. Breakdown of feldspar, volume gain and lateral mass transfer during mylonitization of granitoid in a low metamorphic grade shear zone. *Journal of Structural Geology*, **20**, 175–193.

HIPPERTT, J. & EGYDIO-SILVA, M. 1996. New polygonal grains formed by dissolution–redeposition in quartz mylonite. *Journal of Structural Geology*, **18**, 1345–1352.

JEFFERIES, S. P., HOLDSWORTH, R. E., WIBBERLEY, C. A. J., SHIMAMOTO, T., SPIERS, C. J., NIEMEIJER, A. R. & LLOYD, G. E. 2006. The nature and importance of phyllonite development in crustal scale fault cores: an example from the Median Tectonic Line, Japan. *Journal of Structural Geology*, **28**, 220–235.

KARATO, S.-I. 1988. The role of recrystallization in the preferred orientation of olivine. *Physics of the Earth and Planetary Interiors*, **51**, 107–122.

KURZ, W., FRITZ, H., TENCZER, V. & UNZOG, W. 2002. Tectonometamorphic evolution of the Koralm Complex (Eastern Alps): constraints from microstructures and textures of the 'Plattengneis' shear zone. *Journal of Structural Geology*, **24**, 1957–1970.

KRONENBERG, A. K. & TULLIS, J. 1984. Flow strengths of quartz aggregates: grain size and pressure effects due to hydrolytic weakening. *Journal of Geophysical Research*, **89**, 4281–4297.

LAW, R. D. 1990. Crystallographic fabrics: a selective review of their applications to research in structural geology. *In*: KNIPE, R. J. & RUTTER, E. H. (eds) *Deformation Mechanisms, Rheology and Tectonics*. Geological Society, London, Special Publications, **54**, 335–352.

LAW, R. D., CASEY, M. & KNIPE, R. J. 1986. Kinematic and tectonic significance of microstructure and crystallographic fabrics within quartz mylonites from the Assynt and Eriboll regions of the Moine thrust zone, NW Scotland. *Transactions of the Royal Society of Edinburgh, Earth Sciences*, **77**, 99–125.

LAW, R. D., SCHMID, S. M. & WHEELER, J. 1990. Simple shear deformation and crystallographic fabrics: a possible natural example from the Torridon area of NW Scotland. *Journal of Structural Geology*, **12**, 29–45.

LAW, R. D., SEARLE, M. P. & SIMPSON, R. L. 2004. Strain, deformation temperatures and vorticity of flow at the top of the Greater Himalayan Slab, Everest Massif, Tibet. *Journal of the Geological Society, London*, **161**, 305–320.

LEBENSOHN, R. A. & TOMÉ, C. N. 1993. A self-consistent anisotropic approach for the simulation of plastic deformation and texture development of polycrystals: application to zirconion alloys. *Acta Metallurgica et Materialia*, **41**, 2611–2624.

LINKER, M. F., KIRBY, S. H., ORD, A. & CHRISTIE, J. M. 1984. Effects of compression direction on the plasticity and rheology of hydrolytically weakened synthetic quartz crystals at atmospheric pressure. *Journal of Geophysical Research*, **89**, 4241–4255.

LISTER, G. S. & HOBBS, B. E. 1980. The simulation of fabric development during plastic deformation and its application to quartzite: the influence of deformation history. *Journal of Structural Geology*, **2**, 355–370.

LISTER, G. S. & PATERSON, M. S. 1979. The simulation of fabric development during plastic deformation and its application to quartzite: fabric transitions. *Journal of Structural Geology*, **1**, 99–115.

LISTER, G. S. & WILLIAMS, P. F. 1979. Fabric development in shear zones: theoretical controls and observed phenomena. *Journal of Structural Geology*, **1**, 283–298.

LISTER, G. S., PATERSON, M. S. & HOBBS, B. E. 1978. Simulation of fabric development during plastic deformation and its application to quartzite: model. *Tectonophysics*, **45**, 107–158.

LLOYD, G. E. 2004. Microstructural evolution in a mylonitic quartz simple shear zone: the significant roles of dauphine twinning and misorientation. *In*: ALSOP, G. I., HOLDSWORTH, R. E., MCCAFFREY, K. & HANDY, M. (eds) *Transports and Flow Processes in Shear Zones*. Geological Society, London, Special Publications, **224**, 39–61.

LLOYD, G. E. & FREEMAN, B. 1994. Dynamic recrystallisation of quartz and quartzites. *Journal of Structural Geology*, **16**, 867–881.

LLOYD, G. E. & KENDALL, J.-M. 2005. Petrofabric derived seismic properties of a mylonitic quartz simple shear zone: implications for seismic reflection profiling. *In*: HARVEY, P. K., BREWER, T., PEZARD, P. A. & PETROV, V. A. (eds) *Petrophysical Properties of Crystalline Rocks*. Geological Society, London, Special Publications, **240**, 75–94.

LLOYD, G. E., LAW, R. D., MAINPRICE, D. & WHEELER, J. 1992. Microstructural and crystal fabric evolution during shear zone formation. *Journal of Structural Geology*, **14**, 1079–1100.

MAINPRICE, D. H. 1981 *The experimental deformation of quartz polycrystals*. PhD thesis. Australian National University, Canberra.

Mainprice, D. & Paterson, M. S. 1984. Experimental studies on the role of water in the plasticity of quartzites. *Journal of Geophysical Research*, **89**, 4257–4269.

Mainprice, D. H. & Paterson, M. S. 2005. Experimental deformation of flint in axial compression. *In*: Bruhn, D. & Burlini, L. (eds) *High Strain Zones: Structure and Physical Properties*. Geological Society, London, Special Publications, **245**, 251–276.

Mainprice, D. & Jaoul, O. 2009. A transmission electron microscopy study of experimentally deformed quartzite with different degrees of doping. *Physics of Earth and Planetary Interiors*, **172**, 55–66.

McLaren, A. C. 1991. *Transmission Electron Microscopy of Minerals and Rocks*. Cambridge University Press, New York.

Menegon, L., Piazolo, S. & Pennacchioni, G. 2010. The effect of Dauphiné twinning on plastic strain in quartz. *Contributions to Mineralogy and Petrology*, **161**, 635–652. doi: 10.1007/s00410-010-0554-7.

Molinari, A., Canova, G. R. & Azhy, S. 1987. A self-consistent approach of the large deformation polycrystal viscoplasticity. *Acta Metallurgica*, **35**, 2983–2994.

Nicolas, A. & Poirier, J.-P. 1976. *Crystalline Plasticity and Solid State Flow in Metamorphic Rocks*. John Wiley & Sons, New York.

Okudaira, T., Takeshita, T., Hara, I. & Ando, J. 1995. A new estimate of the conditions for transition from basal to prism [c] slip in naturally deformed quartz. *Tectonophysics*, **250**, 31–46.

Pennacchioni, G., Menegon, L., Leiss, B., Nestola, F. & Bromiley, G. 2010. Development of crystallographic preferred orientation and microstructure during plastic deformation of natural coarse-grained quartz veins. *Journal of Geophysical Research*, **115**, B12405, doi: 10.1029/2010JB007674.

Poirier, J.-P. 1985. *Creep of Crystals: High Temperature Deformation Processes in Metals, Ceramics and Minerals*. Cambridge University Press, Cambridge, UK.

Poirier, J.-P. & Nicolas, A. 1975. Deformation induced recrystallization due to progressive misorientation of subgrains with special reference to mantle peridotites. *Journal of Geology*, **83**, 707–720.

Ralser, S., Hobbs, B. E. & Ord, A. 1991. Experimental deformation of a quartz mylonite. *Journal of Structural Geology*, **13**, 837–850.

Ramsay, J. G. 1967. *Folding and Fracturing of Rocks*. McGraw-Hill Book Co., New York.

Ramsay, J. G. & Graham, R. H. 1970. Strain variation in shear belts. *Canadian Journal of Earth Sciences*, **7**, 786–813.

Ribe, N. M. 1989. A continuum theory for lattice preferred orientation. *Geophysical Journal*, **97**, 199–207.

Rutter, E. H. & Brodie, K. H. 2004. Experimental intracrystalline plastic flow in hot-pressed synthetic quartzite prepared from Brazilian quartz crystals. *Journal of Structural Geology*, **26**, 259–270.

Sachs, G. 1928. Zur Ableitung einer Fliessbedingung. *Zeichschrift der Verein deutscher Ingenieur*, **72**, 734–736.

Schmid, S. M. & Casey, M. 1986. Complete fabric analysis of some commonly observed quartz *c*-axis patterns. *In*: Hobbs, B. E. & Heard, C. (eds) *Mineral and Rock Deformation: Laboratory Studies – The Paterson Volume*. American Geophysical Union, Geophysical Monograph, **36**, 263–286.

Stipp, M., Stünitz, H., Heilbronner, R. & Schmid, S. M. 2002. The eastern Tonale fault zone: a 'natural laboratory' for crystal plastic deformation of quartz over a temperature range from 250 to 700°C. *Journal of Structural Geology*, **24**, 1861–1884.

Takeshita, T. 1996. Estimate of physical conditions for deformation based on *c*-axis transitions in naturally deformed quartzite. *Journal of the Geological Society of Japan*, **102**, 211–222.

Takeshita, T. & Wenk, H.-R. 1988. Plastic anisotropy and geometrical hardening in quartzites. *Tectonophysics*, **149**, 345–361.

Takeshita, T., Wenk, H.-R. & Lebensohn, R. 1999. Development of preferred orientation and microstructure in sheared quartzite: comparison of natural data and simulated results. *Tectonophysics*, **312**, 133–155.

Taylor, G. I. 1938. Plastic strain in metals. *Journal of the Institute of Metals*, **62**, 301–324.

Tomé, C. N. & Lebensohn, R. 2004. Self consistent homogenization methods for texture and anisotropy. *In*: Raabe, D., Roters, F., Barlat, F. & Chen, L.-Q. (eds) *Continuum Scale Simulation of Engineering Materials: Fundamentals – Microstructures – Process Applications*. J. Wiley & Sons, New York, 462–489.

Tommasi, A., Mainprice, D., Canova, G. & Chastel, Y. 2000. Viscoplastic self-consistent and equilibrium-based modeling of olivine lattice preferred orientations: implications for the upper mantle seismic anisotropy. *Journal of Geophysical Research, Solid Earth*, **105**, 7893–7908.

Toy, V. G., Prior, D. J. & Norris, R. J. 2008. Quartz textures in the Alpine fault mylonites: influence of pre-existing preferred orientations on fabric development during progressive uplift. *Journal of Structural Geology*, **30**, 602–621.

Trépied, L., Doukhan, J. C. & Paquet, J. 1980. Subgrain boundaries in quartz: theoretical analysis and microscopic observations. *Physics and Chemistry of Minerals*, **5**, 201–218.

Trepmann, C. A. & Stöckhert, B. 2003. Quartz microstructures developed during non-steady state plastic flow at rapidly decaying stress and strain rate. *Journal of Structural Geology*, **25**, 2035–2051.

Trimby, P. W., Prior, D. J. & Wheeler, J. 1998. Grain boundary hierarchy development in a quartz mylonite. *Journal of Structural Geology*, **20**, 917–935.

van Daalen, M., Heilbronner, R. & Kunze, K. 1999. Orientation analysis of localized shear deformation in quartz fibres at the brittle–ductile transition – deformation mechanisms in nature and experiment. *Tectonophysics*, **302**, 83–107.

Vernooij, M. G. C., den Brok, B. & Kunze, K. 2006. Development of crystallographic preferred orientations by nucleation and growth of new grains in experimentally deformed quartz single crystals. *Tectonophysics*, **427**, 35–53.

Wallis, S. R. 1995. Vorticity analysis and recognition of ductile extension in the Sanbagawa belt, SW Japan. *Journal of Structural Geology*, **17**, 1077–1093.

WENK, H.-R. & CHRISTIE, J. M. 1991. Comments on the interpretation of deformation textures in rocks. *Journal of Structural Geology*, **13**, 1091–1110.

WENK, H.-R., CANOVA, G., MOLINARI, A. & KOCKS, U. F. 1989. Viscoplastic modeling of texture development in quartzite. *Journal of Geophysical Research*, **94**, 17895–17906.

WHITE, S. H. 1979. Grain and subgrain size variations across a mylonite shear zone. *Contributions to Mineralogy and Petrology*, **70**, 193–202.

WIBBERLEY, C. A. J. 1999. Are feldspar-to-mica reactions necessarily reaction-softening processes in fault zones? *Journal of Structural Geology*, **21**, 1219–1227.